ABSTRACT

Title of Dissertation:
TUNABLE ATOMIC LINE MONOCHROMATORS FOR BRILLOUIN SPECTROSCOPY

Romanus J. Hutchins,
Doctor of Philosophy, 2024

Dissertation directed by:
Professor Giuliano Scarcelli,
Department of Bioengineering

Brillouin microscopy, a non-contact, spatially-resolved imaging method, provides insights into the mechanical information of samples. The first generation of Brillouin microscopes combined confocal microscopes and etalon-based spectrometers. In this setup, a confocal microscope scans a laser across the sample pixel-by-pixel, while the etalon spectrometer measures the Brillouin shift frequency at each pixel. Despite the extended image acquisition times in biological samples (>20 ms/pixel), advancements have been made in the field to enhance the overall speed of Brillouin imaging. For example, line-scan Brillouin spectrometers use orthogonal detection to measure the Brillouin scattering at a row of pixels in a single shot. The pixel multiplexing in one-dimension (1D) improved the Brillouin imaging speeds 20-fold. Further multiplexing to two dimensions, or full-field spectroscopy, where the frequency domain is sequentially acquired but all the pixels in the field of view are simultaneously measured at each frequency, can further improve the average image acquisition time. However, there are currently no solutions for sub-picometer (sub-GHz) spectral resolution, two-dimensional (2D) multiplexing of Brillouin images.

Here, I use the laser induced circular dichroism (LICD) effect in atomic vapors to create monochromators for 2D multiplexing at high spectral resolutions. These atomic line monochromators possess spectral resolutions dependent on the linewidth of the atomic resonance (~MHz), and they are ideal for pixel multiplexing because they have spectral analysis capabilities that do not depend on the spatial separation of spectral components. First, I present a full characterization of a tunable atomic line monochromator. I measure the transmission, spectral resolution, and spectral tunability of the device, as well as demonstrate whole-image transmission through the atomic line monochromator. Next, for practical implementations of the device to Brillouin spectroscopy, I created an atomic line monochromator based on a ladder-type atomic transition. This iteration of the device suffers from less noise than the previous version, leading to the first Brillouin measurements with this device. Finally, I present the first full-field Brillouin microscope by demonstrating whole Brillouin imaging with orthogonal detection with an atomic line monochromator.

TUNABLE ATOMIC LINE MONOCHROMATORS FOR BRILLOUIN SPECTROSCOPY

by

Romanus Hutchins

Dissertation submitted to the Faculty of the Graduate School of the
University of Maryland, College Park, in partial fulfillment
of the requirements for the degree of
Doctor of Philosophy
2024

Advisory Committee:
  Professor Giuliano Scarcelli, Chair
  Professor Neil Blough
  Professor Ian White
  Professor Jenna Mueller
  Professor Yang Tao

“I have been in Sorrow’s kitchen and licked out all the pots. Then I have stood on the peaky mountain wrapped in rainbows, with a harp and sword in my hands.”

- Zora Neal Hurston

Dedications

To my parents, Riccardo and Jeanine Hutchins: Nothing I have ever done or will ever do would be possible without your unwavering support for my education and your unconditional love for me. My spirit is imbued with the resilience and joy I have witnessed from both of you throughout my life.

To my brother and sister, Raphael and Razia: You have been the guiding stars of my life. Jake, your wisdom beyond your years encourages me to strive for betterment. Razia, your unyielding courage has always ignited hope within me. Witnessing your greatness has been a constant source of inspiration, and I am grateful to have both of you as confidants.

To the rest of my family: I am thankful to come from such a loving group of people. Your contributions to my life, no matter how big or small, will always leave a substantial impression upon my heart. It truly does take a village to raise a child.

Acknowledgements

I would first like to express my sincerest gratitude to my graduate mentor, Dr. Giuliano Scarcelli, whose strong commitment to excellence challenged me to exceed my own expectations. I benefited immensely from his rigorous guidance and constructive feedback, which has played an important role in my development as a scientist. Equally significant is his constant support and dedication, coupled with a balance of rigor and kindness that characterizes his mentorship. Despite the challenges of academic research, Giuliano’s compassionate approach fostered a supportive learning environment that greatly contributed to my growth and success. I am truly grateful for his profound impact on my academic journey.

I would like to express my gratitude to my dissertation committee members. Their insightful advice and steadfast support have greatly enhanced the quality of my dissertation work.

I would also like to thank my incredibly talented lab mates, for their support and friendship: Dr. Jitao Zhang, Dr. Giulia Zanini, Dr. Yogeshwari Ambekar, Dr. Hongyuan Zhang, Dr. Eitan Edrei, Dr. Antonio Fiore, Dr. Joshua Webb, Dr. Christina Conrad, Dr. Miloš Nikolić, Dr. Xuewen Zhou, Stephanie Lashley, Eric Frank, Chenchen Handler, Raymundo Rodríguez-López, Jake Rosvold (affectionately known to me as White Romanus), and Justin Schumacher. I am fortunate to have worked with such a kind and generous group of people.

I would like to give a special thanks to the lab mates who played significant roles in the completion of my dissertation. Dr. Yogeshwari Ambekar, your arrival to the lab was kismet, as your positive attitude and patience was fundamental to the realization of Full-Field Brillouin microscopy and the completion of my dissertation. To Eric Frank and Justin Schumacher: I could not have seen my first Brillouin photons without our fellowship. I have never had more fun in my academic career, from pre-school to graduate school, than I had when the three of us worked together. I must also extend a special thanks to Dr. Giulia Zanini. You have been a constant beacon of support and scholastic greatness for me. Watching your diligence in the lab was paramount to my success, so much so that an entirely new dissertation can be written compiling all of the lessons that I have learned from you. Perhaps the most important lesson was learned outside of the lab, however, where I witnessed your dedication to nurturing meaningful personal relationships and your hobbies.

Finally, I would like to thank the Clark Doctoral Fellowship and the Ann G. Wylie Fellowship for providing me the resources to successfully complete my dissertation.

Table of contents

List of Abbreviations

^{87}Rb:	Rubidium-87
^{85}Rb:	Rubidium-85
ASE:	Amplified Spontaneous Emission
CO:	Cross-Over peaks
FADOF:	Faraday Anomalous Dispersion Optical Filter
FOV:	Field of View
FP:	Fabry-Pérot
FWHM:	Full Width at Half Maximum
LICD:	Laser Induced Circular Dichroism
PSF:	Point Spread Function
SBR:	Signal-to-Background Ratio
SNR:	Signal-to-Noise Ratio
VIPA:	Virtually Imaged Phased Array

List of Figures

Chapter 1

Introduction

1.1 Brillouin microscopy

1.1.1 Brillouin scattering

Brillouin scattering is the phenomenon that occurs when incident photons are scattered by the phonons of a material. Phonons are thermally generated acoustic waves that travel at the speed of sound v within the material. Brillouin scattering was first reported by Léon Brillouin in 1922 [1], and the first experimental demonstration of Brillouin scattering was made by Evengi Gross in 1930 [2]. Although the visualization of Brillouin scattering was limited to applications in the material sciences, recent technological advancements have led to its use in biology.

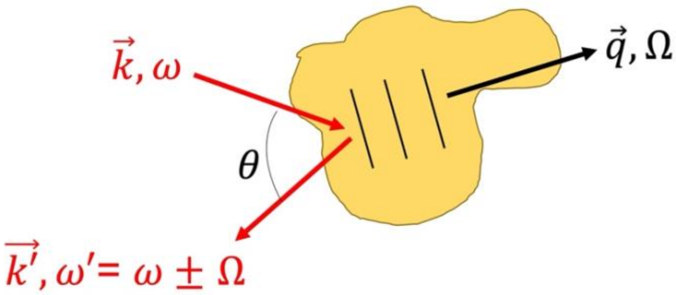

Figure 1.1. Schematic of Brillouin scattering.

The photon-phonon interaction can be described using Fig 1.1. The propagation of an incoming photon of frequency ω can be described by wavevector $|\boldsymbol{k}|$

$$|\boldsymbol{k}| = \frac{\omega \cdot n}{c} \tag{1.1}$$

where n is the index of refraction and c is the speed of light. When the incoming photons are scattered by phonons, the scattered light has a frequency ω' and wavevector $|\boldsymbol{k}'|$. Due to the conservation of energy and momentum, ω' and $|\boldsymbol{k}'|$ are

$$\omega' = \omega \pm \Omega \tag{1.2}$$

$$|\boldsymbol{k}'| = |\boldsymbol{k}| \pm |\boldsymbol{q}| \tag{1.3}$$

where $|\boldsymbol{q}|$ is the phonon wavevector can and Ω is the frequency of the phonon. Ω is related to $|\boldsymbol{q}|$ and ν according to the linear dispersion relation

$$\Omega = \nu \cdot q = \sqrt{M/\rho} \cdot q \tag{1.4}$$

where M is the material longitudinal modulus and ρ is the material density. Because $\omega >> \Omega$, making $|\boldsymbol{k}|$ and $|\boldsymbol{k}'|$ nearly equal, we can estimate $|\boldsymbol{q}|$ to be

$$|\boldsymbol{q}| = 2|\boldsymbol{k}| \sin\left(\frac{\theta}{2}\right) = 2n\frac{\omega}{c}\sin\left(\frac{\theta}{2}\right) \tag{1.5}$$

where θ is the angle between the axis of observation of Brillouin scattered photons and the axis of the incoming light. Substituting Eq. (1.5) into Eq. (1.4), we get a new equation for Ω

$$\Omega = 2n\frac{\omega}{c}\,v\sin\left(\frac{\theta}{2}\right) = 2n\frac{\omega}{c}\sqrt{M/\rho}\cdot\sin\left(\frac{\theta}{2}\right) \tag{1.6}$$

which is known as the Brillouin shift and is how much the Brillouin scattered light has changed in frequency from the incident photon frequency. From this treatment, we can see that the Brillouin shift is proportional to the speed of sound within the material, and therefore proportional to the longitudinal modulus of the material.

1.1.2 Brillouin spectrometer instrumentation

An illustration of a characteristic Brillouin spectrum can be seen in Fig. 1.2. The middle peak corresponds to the elastically scattered, or Rayleigh scattered, light (i.e., the photons that did not experience an energy change during the scattering event). The outer peaks correspond to the Brillouin scattered photons. The Anti-Stokes peak coincides with photons that lost energy in the scattering event, and the opposite is true for the Stokes shift. The Brillouin spectrum of different materials can be visualized using dispersive elements such as interferometers or etalons. Although the three characteristic peaks are shown as an illustration in Fig. 1.2, in real cases the peak from the Rayleigh peak can sometimes be more intense than the two Brillouin peaks due to reflections in the optics and Mie scattering [3]. The Brillouin scattering cross-section is 10^{-9}-10^{-10} in biological samples, meaning that one in one billion photons are scattered by phonons in a single scattering event. Due to the low scattering efficiency of Brillouin scattering, Brillouin spectrometers require high throughput (or transmission), which is the ratio between the number of photons you measure versus the number of photons that are being sent to the spectrometer. The intensity of the nearby Rayleigh peak necessitates high spectral extinction, which is the ratio between the background intensity and the signal intensity through the spectrometer. Lastly, the spectrometer must have sub-GHz resolution because the Brillouin shift can be between 3-10 GHz and the linewidth can be 150-400 MHz depending on the sample. For example, for 532 nm illumination and 180^o detection, the Brillouin shift of water is 7.44 GHz and 500 MHz linewidth [4].

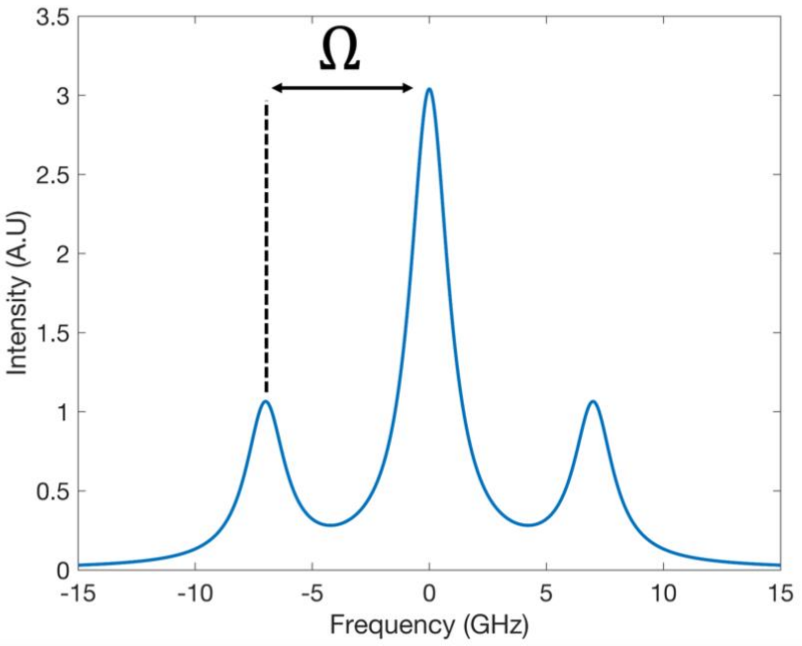

Figure 1.2. Exemplary Brillouin spectrum.

The first generation of Brillouin spectrometers used Fabry-Pérot (FP) etalons to measure Brillouin scattered light due to their high spectral extinction. An FP cavity is made of two partially reflective mirrors. The light inside of the cavity rebounds between both mirrors and there is only transmission outside of the cavity when the light inside of the cavity meets a resonance condition that matches the cavity length. By scanning the FP cavity, the Brillouin spectrum of light can be collected. In 1970, J.R. Sandercock used a double-pass FP interferometer to reach 60dB spectral extinction [5]. The system gains higher extinction with each pass in through the FP cavity.

The benefit of using FP interferometers for Brillouin spectroscopy is the high spectral resolution and extinction. However, the tandem FP Brillouin spectrometer suffered from low transmission because there is a tradeoff between spectral resolution and transmission due to the high reflectivity of the cavity mirrors [6]. Virtually imaged phase arrays (VIPAs) are etalons that are very similar to FPs [3, 7]. VIPAs are cavities, but one of the mirrors is highly reflective with a transparent window at the bottom for light to be injected, and the other mirror (the output mirror) is partially reflective. When the VIPA is at an angle, the input light is rebounded in the cavity constructive interference occurs at an angle depending on the wavelength of the signal. The constructive interference for difference frequency components occurs at different angles, making it so that wavelengths of light are separated in space. Using a lens, the spectrum of the signal can be recorded in a single shot. A single VIPA carries roughly 30 dB extinction and ~80% throughput [3]. The cross-axis Brillouin spectrometer was invented so that Brillouin signal could travel through two VIPAs to increase the spectral extinction. The cross-axis VIPA Brillouin spectrometer can achieve upwards of 80 dB extinction with >1 GHz spectral resolution and more than three times the throughput of a tandem FP spectrometer [7].

1.1.3 Brillouin microscopes

Before employing VIPA etalons, Brillouin spectroscopy did not possess the performances to measure biological samples. The FP-based Brillouin spectrometers acquired the Brillouin spectrum by raster scanning the FP etalon cavity, which led to long acquisition times that could lead to tissue photodamage. Once VIPAs were incorporated into Brillouin spectrometers, the technology was finally fast enough because the spectrum could be acquired in a single shot. The VIPA-based Brillouin spectrometer was combined with a confocal microscope to create Brillouin microscopy. With Brillouin microscopy, a confocal microscope a sample is raster scanned across a fixed laser spot pixel by pixel and the Brillouin spectrometer is used to measure the Brillouin shift at each pixel (Fig. 1.3(a)). Brillouin microscopy is label-free, all optical longitudinal technique. Using the Brillouin shift as a contrast mechanism provides insight into the local material longitudinal modulus.

Existing designs of Brillouin spectrometers have approached the fundamental speed limit for high SNR in biological samples, thereby necessitating the development of new methods to enhance the speed of Brillouin microscopy. In this regard, multiplexed analysis of the Brillouin spectra appears to be a promising pathway. Using line illumination to multiplex Brillouin pixels significantly reduced the image acquisition time for Brillouin images (Fig. 1.3(b)). A pencil beam illuminates a sample and a Brillouin spectrometer collects Brillouin scattered light orthogonally to the line of illumination, allowing for the simultaneous spectral analysis of pixels in a single row [8-10]. Further multiplexing to two dimensions (2D), or full-field spectroscopy, where the frequency domain is sequentially acquired but all the pixels in the field of view are simultaneously measured at each frequency, can further improve the imaging speed. However, while full-field spectral scanning is straightforward in spectroscopy techniques requiring low spectral resolution [11-16]; for Brillouin scattering spectroscopy, which requires sub-picometer (sub-GHz) spectral resolution, no solution for 2D multiplexing currently exists.

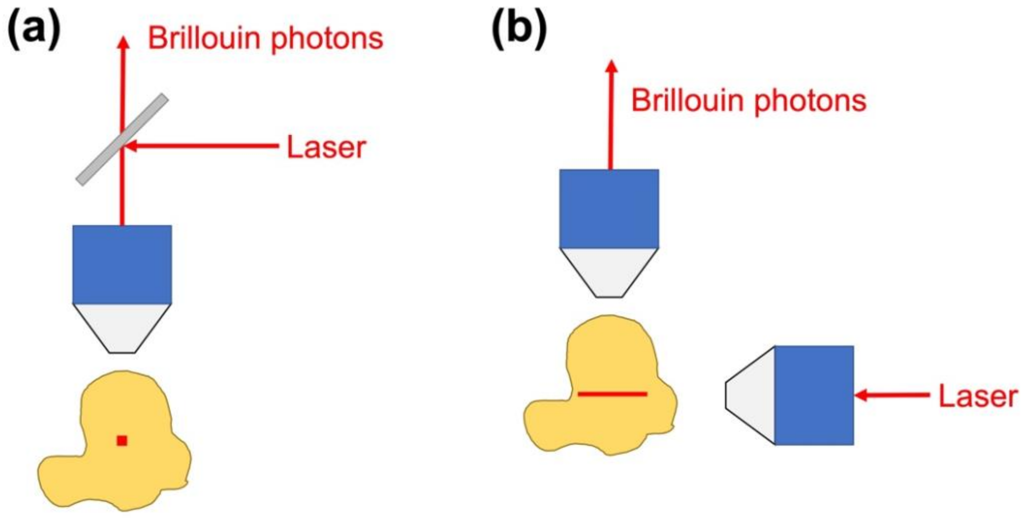

Figure 1.3. Brillouin microscope illumination configurations.(a) Point-scan configuration. (b) Line-scan configuration.

1.2 Atomic line monochromators

In this section, the working principle and transmission characteristics of an atomic line monochromator will be analyzed. A brief overview of the technology will be provided, followed by derivation of the transmission coefficient for a typical atomic line monochromator. Finally, the monochromator transmission will be calculated using the classical theory of the optical absorption coefficients for the two orthogonal circular polarization components when one of the coefficients undergoes saturated absorption.

1.2.1 Overview

The dispersive properties of atomic vapors have been used to create ultranarrow bandpass monochromators with a wide field of view (FOV) for spectral analysis. Atomic vapors are gaseous media where the vapor is made of an atomic species such as potassium, cesium, or rubidium. In the presence of an external field such as a magnetic field or an electromagnetic field, the absorptive properties of atoms in the vapor will change for different polarizations of incoming light. These so-called atomic line monochromators are created by placing an atomic vapor between two crossed linear polarizers. When signal light is transmitted through the atomic line monochromator, the signal will be linearly polarized in the direction of the input polarizer. The atomic vapor prepared by the external field will shift the polarization of the signal near the very narrow atomic resonance, creating transmission through the output linear polarizer that is crossed with the input polarizer. The result is a monochromator with spectral resolution < 1GHz, orders of magnitude greater than conventional interference filters. Furthermore, atomic line monochromators possess wide FOVs because they use vapors for spectral analysis.

An example of an atomic line monochromator is the Faraday anomalous dispersion optical filter (FADOF) [17-25]. FADOFs use an external magnetic field to split degenerate atomic resonances into separate components, a phenomenon called

Zeeman splitting [26]. The Zeeman splitting creates a circular dichroism effect within the atomic vapor near the atomic resonance. When incoming linearly polarized light is transmitted through the prepared vapor, because the linearly polarized light has equal parts of right and left circular polarization components, the atomic vapor will absorb the two orthogonal circular polarizations differently. As a result of the Zeeman splitting, the polarization of linearly polarized light near resonance will be flipped, causing transmission past the downstream polarizer, creating an ultra-narrow bandpass monochromator. FADOFs have been used in applications such as LIDAR systems [18-20] space communications [21,22], and laser frequency locking [23-35].

Devices like FADOF that do not use spectral dispersion for analysis are attractive for applications in Brillouin spectroscopy because they have a spectral resolution (.5-1 GHZ) and throughput (~50%) like VIPA-based Brillouin spectrometers while having the ability to perform full-field spectral analysis. A type of FADOF based on the excited states of rubidium (ESFADOF) was used as an edge filter to study the temperature profiles of water by measuring the Brillouin shift [19]. However, FADOF technology is not ideal for Brillouin measurements due to the inherent limitation of FADOFs, which typically exhibit multi-band transmission spectra. This arises from the global effects of the magnetic field on multiple atomic resonances of the vapor. The frequency range of these resonances can span from several GHz. This limitation hinders the selectivity of the device, making it less suitable for Brillouin measurements.

1.2.2 Atomic line monochromator transmission coefficient

Consider an atomic vapor cell sandwiched between two crossed linear polarizers, where the first polarizer has the transmission oriented in the *x*-direction and the second polarizer has the transmission axis oriented in the *y*-direction (Fig. 1.4). A weak probe beam, i.e., the laser beam to be spectrally analyzed, will counter-propagate with a pump beam inside of the cell in the *z*-direction.

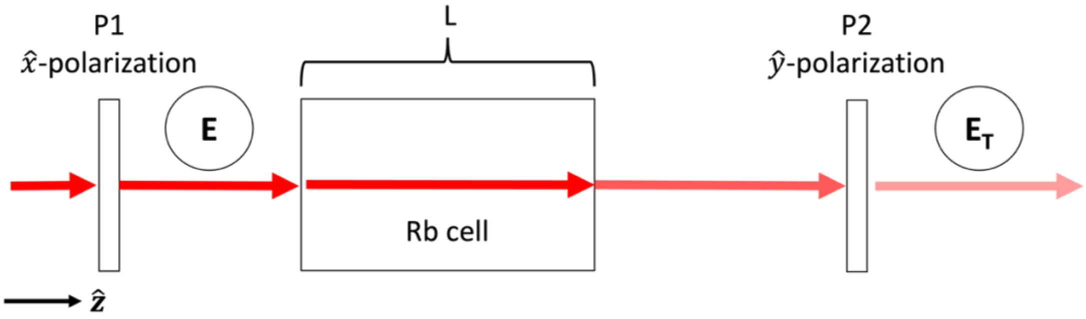

Figure 1.4. Schematic drawing of an atomic line monochromator.

Before entering the cell, the linearly polarized probe light will have an electric field vector *E*

$$\hat{E} = E_0 \hat{x} e^{\alpha z} = \frac{E_0}{\sqrt{2}} (\widehat{\sigma_+} e^{\alpha_+ z} + \widehat{\sigma_-} e^{\alpha_- z}) \tag{1.7}$$

where α is the absorption coefficient and α_+ (α_-) is the absorption coefficient for right (left) circularly polarized light. When the probe is transmitted through the second linear polarizer the transmitted wave is

$$\widehat{E_T} = \frac{E_0}{2}\hat{y}\left(e^{-\frac{\alpha_+}{2}L} - e^{-\frac{\alpha_-}{2}L}\right) \tag{1.8}$$

where L is the length of the atomic vapor cell that both beams overlap inside of the atomic vapor cell. The total transmission past the second polarizer is

$$T = {\left|\widehat{E_T}\right|^2}\Big/{\left|\hat{E}\right|^2}\,. \tag{1.9}$$

To simplify T, it is helpful to make relations for between α_+ and α_-

$$\alpha_0 = \frac{1}{2}(\alpha_+ + \alpha_-) \tag{1.10}$$

$$\Delta\alpha = \frac{1}{2}(\alpha_+ - \alpha_-) \tag{1.11}$$

where α_0 is the mean absorption coefficient of the atomic vapor, and $\Delta\alpha$ is the differential absorption coefficient of the atomic vapor [27–29]. Using these two relations, the transmission becomes

$$T = \frac{1}{2}\exp\,(-\alpha_0 L)\{\cosh(\Delta\alpha L) - 1\} \tag{1.12}$$

Referring to Eq. (1.12), we see that transmission occurs past the second polarizer only when $\Delta\alpha \neq 0$ (i.e., $\alpha_+ \neq \alpha_-$). In other words, there is only transmission when there is circular dichroism, the imbalance between the absorption of the two circular polarizations. The imbalance only occurs within a very narrow spectral region that is smaller than Doppler-broadened linewidth and is ultimately limited by the natural linewidth of the transition. Because the second polarizer blocks the non-resonant light, the simple schematic can be thought of as a high spectral resolution monochromator that transmits light at atomic resonances.

1.2.3 Laser Induced circular dichroism

To create an atomic line monochromator the atomic vapor must achieve a differential absorption of right (σ_+) and left (σ_-) circularly polarized light, an effect otherwise known as circular dichroism [27-29]. While FADOF uses a magnetic field to create circular dichroism within an atomic vapor, circular dichroism can also be created with the vapor by taking advantage of the absorption of electromagnetic radiation due to the selection rules for atomic transitions and saturated absorption [26,30-34]. The selection rules are a set of conditions that govern whether an atomic transition is allowed or forbidden. Suppose we have an atomic energy level E_1 and E_2 (Fig. 1.5). Each energy level is split into different magnetic sublevels. These different magnetic sublevels can be accessed by changing the polarization of light, as governed by the selection rules for the magnetic quantum number *m* and the conservation of angular momentum. For example, linearly (π) polarized light has no angular momentum (Fig. 1.5(a)), so the magnetic quantum number does not change when π-polarized light is absorbed (i.e., $\Delta m = 0$). However, circularly polarized light carries angular momentum. When the electron absorbs the photon, angular momentum is exchanged. The exchange creates a cycling effect between the magnetic sublevels in the ground and excited state until there are no more magnetic sublevels to accessed. For example, the absorption of σ_+-polarized light results in a $\Delta m = +1$ change in magnetic quantum number (Fig. 1.5(b)).

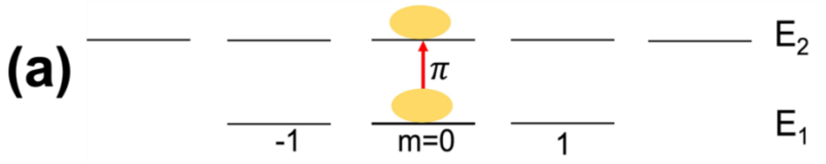

For ***linearly*** polarized light, $\boldsymbol{\Delta m} = \mathbf{0}$

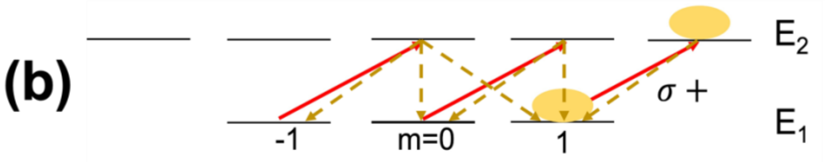

For ***circularly*** polarized light, $\boldsymbol{\Delta m} = \pm\mathbf{1}$

Figure 1.5. Schematic drawing of light absorption to different magnetic sublevels depending on the different polarization of light. (a) When π-

polarized light is on resonance. (b) When σ_+-polarized light is on resonance.

Now, assume a weak, π-polarized signal traverses through an atomic vapor cell and is resonant with one of the atomic transitions. In the absence of an external field, the two orthogonal circular polarization components of the weak signal are absorbed normally. Now, suppose that there is a strong pump laser that is σ_+-polarized, on resonance with the same transition as the weak signal, and is counter-propagating with the signal inside of the atomic vapor cell. Because the laser is σ_+-polarized and is significantly more intense than the weak signal, the pump will create a population of atoms to the atomic energy state with the most angular momentum until light at that transition cannot be absorbed, meaning that the transition is sufficiently saturated. Now that the absorption of σ_+-polarized light has been reduced at that specific atomic transition inside of the vapor, the atomic vapor will absorb the σ_+-polarization component of the signal less than the σ_--polarization component. In other words, the circularly polarized pump laser has made it so that the atomic vapor exhibits circular dichroism, flipping the polarization of incoming π-polarized signal and creating transmission. This effect is called laser induced circular dichroism (LICD), an effect we will use to realize an atomic line monochromator.

The first atomic line monochromator based on the LICD effect was created by Gayen *et al*. in 1995 [35]. Atomic line monochromators based on the LICD effect typically possess 10-20%, <200 MHz bandwidth, and 500-800 GHz frequency tunability [28,29]. Also, because LICD atomic line monochromators use narrow linewidth lasers, the circular dichroism only occurs near a specific resonance, resulting in better spectral resolutions than FADOF systems.

1.2.4 Absorption coefficients for circularly polarized light

From equations 1.10, 1.11, and 1.12, we can see that the signal transmission of the atomic line monochromator depends on the absorbing medium's absorption coefficients for right (α_+) and left (α_-) circularly polarized light. As such, it is necessary to derive the absorption coefficient equations for both circular polarizations. Because the LICD effect requires a circularly polarized pump laser on resonance with a particular atomic transmission, we will choose the pump laser to be right circularly polarized and the absorbing medium to be rubidium-87 (^{87}Rb) at the $5^2S_{1/2}$ ($F_g = 2$, $m_{Fg} = +2$)→$5^2P_{3/2}$ ($F_e = 3$, $m_{Fe} = +3$) transition (780.24 nm). This specific ^{87}Rb transition has been used in the past to create atomic line monochromators [28].

When weak electromagnetic radiation propagates through an absorbing medium, the absorption coefficients α_+ and α_- of the weak signal are

$$\alpha_+(\omega) = \kappa_+(\omega)N_0 \tag{1.13}$$

$$\alpha_-(\omega) = \kappa_-(\omega)N_0 \tag{1.14}$$

where ω is the frequency of the absorbed light, $\kappa_+(\omega)$ is the absorption cross-section for right circularly polarized light, $\kappa_-(\omega)$ is the absorption cross-section for left circularly polarized light, and N_0 is the atomic number density. The absorption cross-section for both circular polarization components is

$$\kappa_{\pm}(\omega) = \frac{f_{\pm}e^2}{4\epsilon_0 m_e c}\left[\frac{\Gamma/2}{(\omega_0 - \omega)^2 + \left(\frac{\Gamma}{2}\right)^2}\right] \tag{1.15}$$

where $f_{\pm}$ is the oscillator strength, e is the electron charge, ϵ_0 is the permittivity of free space, m_e is the electron mass, c is the speed of light, ω_0 is the resonant frequency of the atomic transition of interest, and Γ is the natural linewidth of the trasnition (6 MHz for Rb). The oscillator strength describes the probability of absorption for an atomic transition and is the ratio between the quantum mechanical transition rate and the classical absorption rate [36]. The oscillator strength f_{ge}, which determines the probability of an atomic transition between a ground state (g) and excited state (e) is described as

$$f_{ge} = \left(\frac{8\pi^2 m_e \omega_{ge}}{3he^2}\right)\left|\langle\psi_g|\bar{\boldsymbol{r}}|\psi_e\rangle\right|^2 \tag{1.16}$$

where ω_{ge} is the resonant frequency of the transition, h is Planck's constant, and the term $\left|\langle\psi_g|\bar{\boldsymbol{r}}|\psi_e\rangle\right|^2$ is the Glebsch-Gordan coefficient. The Glebsch-Gordan coefficient is the amplitude of the angular momentum coupling between the ground state and the excited state of an atomic transition and is often tabulated for the atomic transitions of elements like Rb [36]. Because the σ_+-polarized pump laser is resonant with the $5^2S_{1/2}$ (F_g = 2, m_{Fg} = +2)→$5^2P_{3/2}$ (F_e = 3, m_{Fe} = +3) transition, the oscillator strength is calculated to be $f_+ = .0032$. The σ_--polarization component of the probe will undergo the $5^2S_{1/2}$ ($F_g = 2$, $m_{Fg} = +2$)→$5^2P_{3/2}$ ($F_e = 3$, $m_{Fe} = +1$) transition, so the oscillator strength for that transition is calculated to be $f_- = .0013$.

For ^{87}Rb, the atomic number density N_0 is defined as

$$log_{10}(N_0) = 34.8325 + 0.00059T_0 - 3.991log_{10}(T_0) - \frac{4529.6}{T_0} \tag{1.17}$$

where T_0 is the temperature of the atomic vapor [37]. For the case of an atomic vapor cell, the vapor is in equilibrium with condensate inside of the cell. As such, the atomic number density is related to the Clausius-Clapeyron relation. We are only considering the transmission at the center of the transmission, meaning that we will not consider Doppler-broadening for these calculations.

As a result of the right circularly polarized pump beam, the absorption of right circularly polarized light will be reduced in the ^{87}Rb atomic vapor, meaning that the right circular polarization component will undergo saturated absorption. Consequentially, $\alpha_+(\omega)$ becomes

$$\alpha_+(\omega) = \frac{\kappa_+(\omega)N_0}{1 + \left({}^{I}/_{I_{sat}}\right)} \tag{1.18}$$

where I is the pump laser irradiance and I_{sat} is the saturation intensity of the transition [38-40]. I_{sat} is the intensity in which an atom can no longer absorb more light on resonance. For stationary ^{87}Rb atoms, I_{sat} =1.669 mW/cm^2 [28,41].

1.2.5 Transmission characteristics of an LICD atomic line monochromator

With Eq. (1.15) and Eq. (1.18), we now have the absorption coefficients for both orthogonal polarization components necessary to simulate the transmission of an LICD atomic line monochromator. The monochromator transmission is related to the number of atoms inside of the vapor that are sufficiently saturated by the pump laser. In other words, the monochromator transmission is related to the irradiance of the pump laser and the temperature of the atomic vapor.

The LICD atomic line monochromator transmission versus pump irradiance is shown in Fig. 1.6(a). The length of the atomic vapor cell L is 75 mm, and ^{87}Rb vapor at 45^{o}C has an atomic number density $N_0 = 6.1505\times10^{10}$ cm^{-3}. From Fig. 1.6(a), the transmission increases as the pump irradiance increases until saturating near 1.5 W/cm^2, meaning that the pump laser has sufficiently saturated the length of the cell. Notably, the saturation occurs at a transmission T = .25. From Eq. (1.12), the transmission of the LICD atomic line monochromator will not reach higher than 25% because one of the linear polarization components is already blocked by the output polarizer, and only one circular polarization component of the blocked linear polarization is transmitted through the output polarizer. Although the transmission limit is 25%, LICD atomic line monochromators do not reach this limit experimentally because lasers are unable to completely polarize electrons.

The LICD atomic line monochromator transmission versus vapor cell temperature is shown in Fig. 1.6(b). The pump irradiance is held constant at 1 W/cm^2. The monochromator transmission increases as the temperature of the atomic vapor cell increases, reaching ~25% at 45^{o}C. However, the transmission begins to decrease for temperature greater than 45^{o}C. This decrease in transmission is a result of Beer's Law [26]. The temperature of the vapor is so high that the vapor becomes more optically thick at the end of the cell, making it so that the pump laser saturates the vapor less and leading to less transmission of the signal.

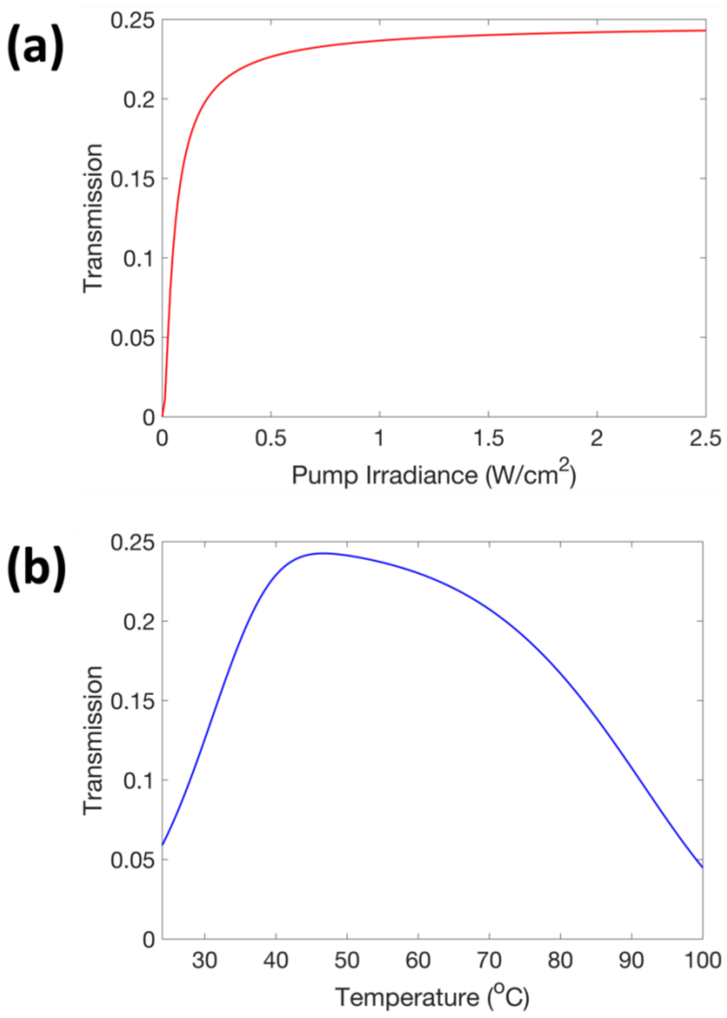

Figure 1.6. Theoretical calculations of the LICD monochromator transmission. (a) Monochromator transmission versus pump irradiance. (b) Monochromator transmission versus atomic vapor cell temperature.

In conclusion, we have identified LICD atomic line monochromators as a technology for measuring Brillouin signal. A classical numerical model has been derived to predict the transmission behaviors of the LICD atomic line monochromator, which agrees with experiments from previous work. The 25% theoretical peak transmission is competitive with current state-of-the-art Brillouin spectrometers. In the future, a more complex model will have to be implemented to predict the transmission characteristics of more complicated pumping schemes, such as a pumping scheme where the circularly polarized pump laser creates circular dichroism at a transition different from the transition it is resonant with. In this case, the atomic number density would be different for the atoms on resonance with the pump laser and the atoms on resonance with the signal at a different frequency.

Chapter 2

Full-field optical spectroscopy at high spectral resolution using atomic vapors*

In this Chapter we report an atomic line monochromator based on the LICD effect and demonstrate the potential of the device for high-resolution, full-field spectroscopy. First, we describe the working principle of the atomic line monochromator using a pump-probe scheme, where the pump laser is used to create the LICD effect inside of the vapor and the probe laser is used to simulate signal. Next, we will characterize the transmission and spectral resolution (or linewidth) performances of the device. We also demonstrate the monochromator frequency scanning range, turning the monochromator into a spectrometer. Finally, we prove the whole-image transmission capabilities of the atomic line monochromator using a USAF target. We then show how LICD effect impacts image contrast and spatial resolution.

---

*The results of this Chapter were part of a peer-reviewed publication, *Optics Express* 31(3), 2023

2.1 LICD atomic line monochromator design

2.1.1 Working principle

Our high-resolution monochromator is based on laser induced circular dichroism (LICD) in rubidium atomic vapors.[1] Consider a rubidium-87 (^{87}Rb) atomic vapor cell and the hyperfine structure of the $5^2S_{1/2} \rightarrow 5^2P_{3/2}$ D_2 line [30]. Fig. 2.1(a) shows all the allowable transitions from ^{87}Rb $5^2S_{1/2}$ ($F_g = 2$) hyperfine ground state to the ^{87}Rb $5^2P_{3/2}$ ($F_e = 1, 2, 3$) hyperfine excited states, as well as the so-called crossover (CO) transitions which are artifacts of the counterpropagating pump and probe beams when traveling atoms see both lasers on resonance when the frequencies are half-way between two hyperfine transitions [26,31]. Fig. 2.1(b) shows the saturated absorption (SAS) spectrum of the ^{87}Rb ($F_g = 2 \rightarrow F_e = 1,2,3$) highlighting the hyperfine transitions and the CO peaks collected using a compact saturation spectroscopy module (CoSy, Toptica).

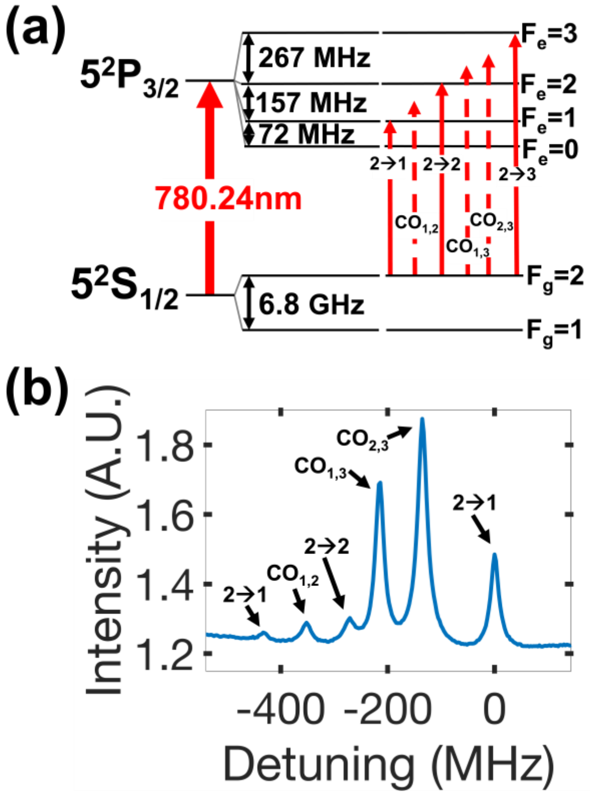

Figure 2.1. Hyperfine transitions of the ^{87}Rb D_2 line. (a) Transition schematic of the D_2 ^{87}Rb $5^2S_{1/2}$ ($F_g = 2$)→ ^{87}Rb $5^2P_{3/2}$ (F_e = 1, 2, 3) along with the crossover (CO) peaks (dashed arrows); (b) SAS spectrum of the D_2 ^{87}Rb $5^2S_{1/2}$ (F_g =2) hyperfine transitions.

When a right-circularly σ_+-pump laser beam is on resonance with the $5^2S_{1/2}$ (F_g = 2)→$5^2P_{3/2}$ (F_e = 3) transition, the atomic population cycles between the magnetic sublevels of ground and excited states, until the transition $5^2S_{1/2}$ (F_g = 2, m_{Fg} = +2)→$5^2P_{3/2}$ (F_e = 3, m_{Fe} = +3) is populated [26,32]. Fig. 2.2(a) shows the atomic transitions and magnetic sublevels of the ^{87}Rb $5^2S_{1/2}$→$5^2P_{3/2}$ D_2 line. When the pump beam is σ_+-polarized, atoms will be excited and make a magnetic sublevel change Δm = +1 . The atoms that accumulate to the excited state will eventually decay from the excited state (Δm = 0, ±1). When the σ_+-polarized pump beam is powerful enough, the atomic population density in the highest magnetic sublevels of ground and excited states becomes the same, hence the transition is saturated, but only for this circular polarization state [28,29]. The pump beam has thus prepared the vapor to absorb the orthogonal circular polarization components differently, an effect known as laser induced circular dichroism (LICD). Fig. 2.2(b) illustrates what happens when a π-polarized probe beam counterpropagating and in resonance with the same hyperfine transition passes through the atomic vapor cell that was prepared by the σ_+-polarized pump beam. The linear polarization of the probe beam can be seen as the superposition of the two orthogonal circular polarization states [33]: the σ_+ component will not be absorbed because the pump laser has saturated the transition and therefore there are no atoms available for absorption; however, according to the selection rules ($\Delta m = -1$), the left-circular polarization component (σ_-) will be absorbed because lower magnetic sublevels in the excited state are free to be occupied.

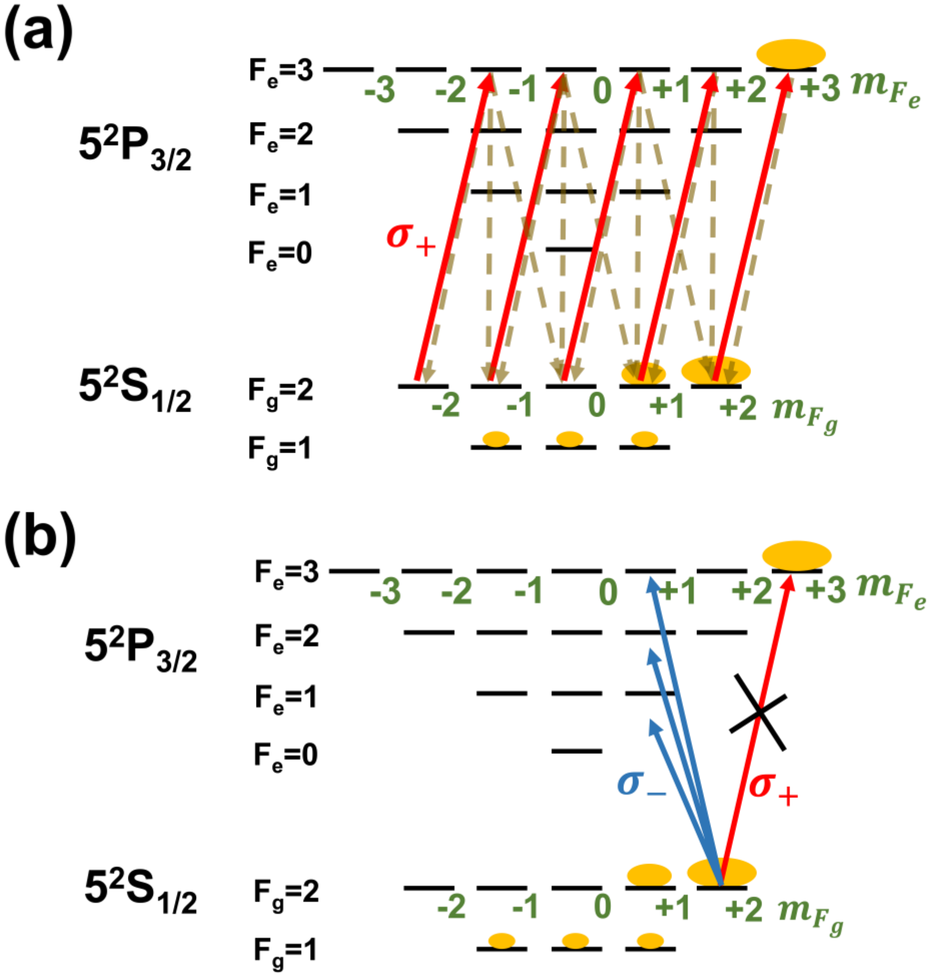

Figure 2.2. Relevant ^{87}Rb transitions and LICD effect. (a) Pump laser saturation scheme. Solid arrows are absorption pathways and dashed arrows are decay pathways; (b) Probe laser absorption after pumping. The specific transitions for the right (left) circular component of the probe are depicted in red (blue).

2.1.2 Experimental setup

The schematic of the experimental setup is shown in Fig. 2.3. The pump laser beam (TA pro, Toptica) is a collimated Gaussian beam with a 1/e^2 diameter of 1.35 mm and is used to prepare the pure ^{87}Rb atomic vapor cell (Precision Glassblowing), which is 75 mm in length and 25 mm in diameter. The pump laser is tunable and can be locked within the D_2 lines of ^{87}Rb and ^{85}Rb using a saturated absorption spectroscopy (SAS) module (CoSy, Toptica). The pump beam laser irradiance is controlled using a half-wave plate (λ/2) and a polarizing beam splitter (PBS) cube. A 10:90 (R:T) non-polarizing beam splitter (BS) cube is used to align the pump laser to propagate through the middle of the atomic vapor cell. The pump beam is σ_+-polarized using a quarter-wave plate (λ/4) before the BS, and its polarization is checked after being reflected by the BS. To simulate spectral analysis, we use a probe laser beam (DL pro, Toptica) that is also a collimated Gaussian beam with a $1/e^2$ diameter of 1.35 mm. The probe beam can also be tuned around and locked within the D_2 lines of the two Rb isotopes using a second CoSy module. The probe beam is focused into the ^{87}Rb cell by an aspherical lens (L1) with a 200 mm focal length f and aligned to counter-propagate with the pump laser inside of the atomic vapor cell. The first Glan-Taylor (GT1) polarizer (100,000:1 extinction ratio) is used to linearly polarize the probe beam before entering the vapor cell. A second aspherical lens (L2) of 200 mm focal length is used to re-collimate the laser and is part of a 4f-system with L1. A second Glan-Taylor polarizer (GT2), crossed with GT1, is placed after the BS and only transmits probe light with frequency falling in the LICD window created by the pump. The extinction of the LICD monochromator is limited by the extinction ratio of the output polarizer, which was measured to be ~-54 dB using an optical power meter (S130C, Thorlabs). The transmitted signal is detected using a photodiode detector (PDA36A2, Thorlabs).

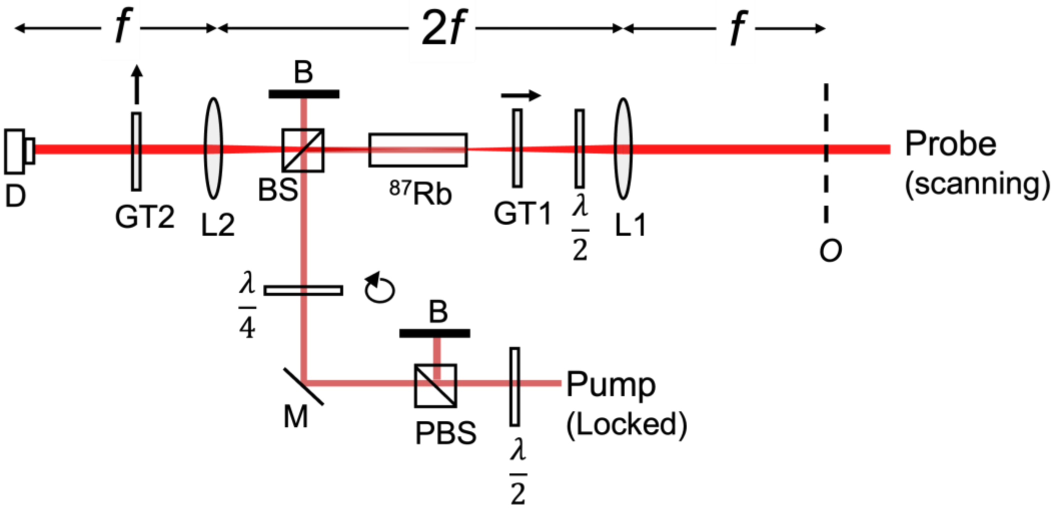

Figure 2.3. Setup schematic: L1, L2, aspherical lenses; GT1, GT2, Glan-Taylor polarizers; BS, non-polarizing beam splitter; M, mirror; PBS, polarizing beam splitter; λ/2, half-wave plate; λ/4, quarter-wave plate; D, detector; B, beam block; *f*, focal length distance of lenses L1 and L2; *O*, object plane 4f system.

2.2 LICD atomic line monochromator characterizations

2.2.1 Transmission and linewidth characterizations

Fig. 2.4. shows an exemplary transmission spectrum of the LICD monochromator (red trace). The probe irradiance is kept at 0.7 mW/cm^2 before entering the ^{87}Rb cell. The laser irradiance of the probe beam is less than the saturation laser irradiance I_{sat} for a stationary ^{87}Rb atom, which is 1.669 mW/cm^2 [28,41]. The temperature of the LICD atomic vapor cell is 42°C. The frequency axis of Fig. 2.4 is calibrated using the CoSy module. The pump irradiance is .7 W/cm^2 and the frequency is locked within the ^{87}Rb ($F_g = 2$) band, and to the CO-2,3 hyperfine transition (see Fig. 2.1), which allowed for the highest LICD induced transmission. The three peaks

correspond to the σ_- transitions $5^2S_{1/2}$ ($F_g = 2$)$\rightarrow$$5^2P_{3/2}$ ($F_e = 1, 2, 3$) (see Fig. 2.2(b)). The transmission peak corresponding to the $5^2S_{1/2}$ ($F_g = 2$)$\rightarrow$$5^2P_{3/2}$ (F_e=3) transition appears due to the saturated absorption induced by the σ_+ pump. The two peaks corresponding to the $5^2S_{1/2}$ ($F_g = 2$)$\rightarrow$$5^2P_{3/2}$ (F_e= 1, 2) are also LICD effects. The σ_- component of the probe on resonance with the two transitions is still normally absorbed, but the σ_+ is not absorbed because there are no more magnetic sublevels in the excited state to satisfy the selection rule for σ_+ transitions, i.e., $\Delta m = +1$. In particular, the highest peak corresponds to the $5^2S_{1/2}$ ($F_g = 2$)$\rightarrow$$5^2P_{3/2}$ ($F_e = 2$) transition, which exhibits the highest magnitude of its Clebsch-Gordan coefficient of the hyperfine dipole matrix ($-\sqrt{1/12}$ for the $5^2S_{1/2}$ (F_g =2 , $m_{Fg} = +2$)$\rightarrow$$5^2P_{3/2}$ ($F_e = 2$, $m_{Fe} = +1$) transition versus $\sqrt{1/30}$ for the $5^2S_{1/2}$ ($F_g = 2$, $m_{Fg} = +2$)$\rightarrow$$5^2P_{3/2}$ ($F_e = 3$, $m_{Fe} = +1$) transition) [28,38]. When the pump is blocked, the probe is absorbed by the vapor and blocked by the crossed polarizer and there is no transmission, as recorded in yellow in Fig. 2.4. The inset of Fig. 2.4 plots transmission converted into decibel (dB) units. Although the polarizers have -54 dB extinction, we will not see the full extinction of the polarizers because it is below the limit of detection for the PDA36A2 photodiode, which is roughly -30dB. Still, the inset shows that when the polarizers are crossed that the rejection is detector limited. The LICD throughput is on the order of 10-20%, consistent with previous experiments [28,29], limited by the collisional effects that the atoms experience.

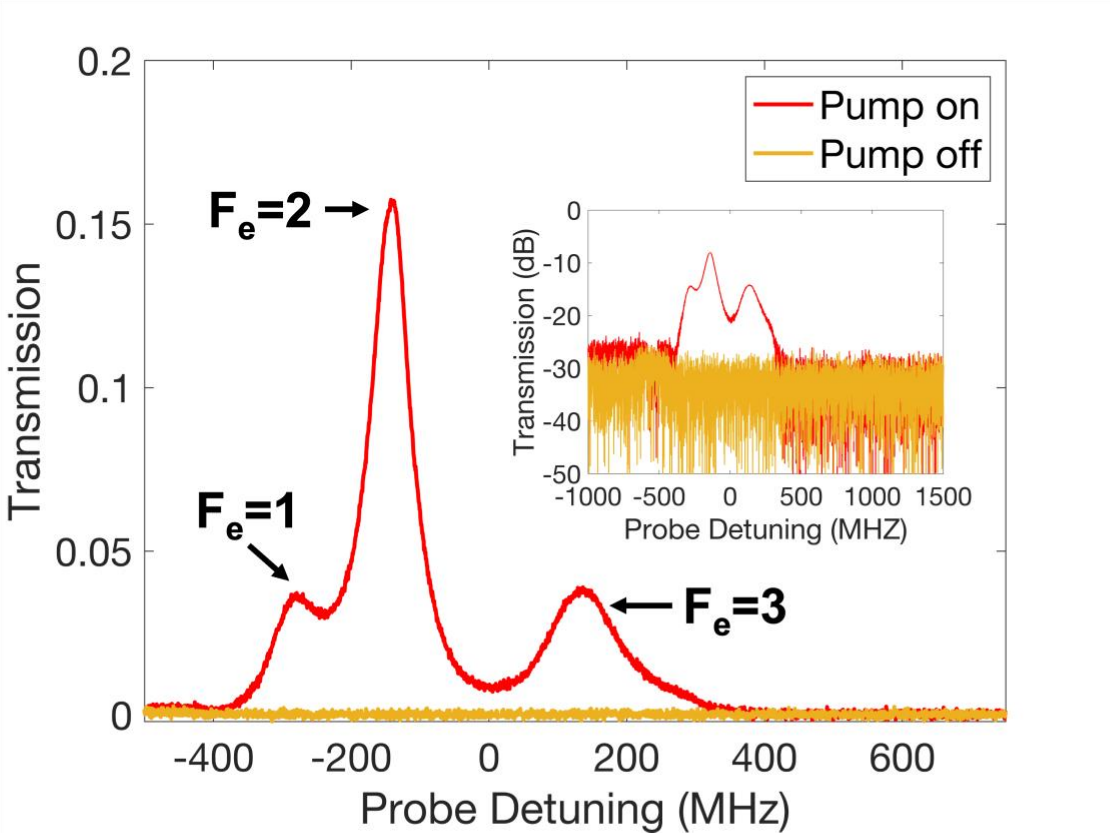

Figure 2.4. Exemplary transmission spectrum of the LICD monochromator. With no pump (yellow line), the linear probe is absorbed by the vapor and blocked by the crossed polarizer. Only in the presence of pump saturation (red line) the monochromator exhibits circular dichroism at specific hyperfine transitions. Inset, LICD transmission and "pump off" condition in units of decibels.

The transmission and the spectral resolution performances of the LICD monochromator are characterized in Fig. 2.5, where amplitude and linewidth (calculated as full width at half maximum, FWHM) of the highest transmission peak are evaluated. These two parameters can be controlled by the number of atoms saturated by the pump laser beam, which in turn can be tuned by the irradiance of the pump laser and the temperature of the vapor cell. Fig. 2.5(a,b) show the behavior of transmission and linewidth versus the pump irradiance when the LICD vapor cell temperature is fixed at 42^{o}C. As the pump becomes more powerful and saturates the transition, the probe transmission increases until there is complete saturation at roughly 1.12 W/cm^2. This power is much higher than I_{sat} reported in [28,37], but it is needed to sufficiently saturate the entire length of the vapor cell at a high temperature. The linewidth of the central peak, which effectively determines the spectral resolution, increases as the pump power increases due to power broadening (Fig. 2.5(b)): the pump beam is so intense that it decreases the lifetime of the transition, which in turn increases the width of the peak [38,39,41]. Fig. 2.5(c,d) show instead the behavior of transmission and linewidth versus the vapor cell temperature when the pump irradiance is fixed at 1.12 W/cm^2. At room temperature, the vapor is in equilibrium with a small portion of ^{87}Rb atoms condensed onto the walls of the cell, thus it is necessary to heat the cell to separate the atoms from the walls of the cell and create a more active gas. As the vapor cell is heated, more atoms become available to be saturated by the pump beam and the transmission increases up until about 45^{o}C (Fig. 2.5(c)). At temperatures higher than 45^{o}C the transmission exhibits a steep decrease. Consistent with Beer’s law [26], the pump beam irradiance decreases and saturates less as it propagates through the absorbing vapor, leading to a decrease in probe transmission. The linewidth instead decreases with the cell temperature (Fig. 2.5(d)) possibly because, as more atoms interact with the lasers, the natural linewidth of the transition can be resolved.

Overall, a compromise must be found between temperature and pump power to achieve a good transmission level and a good spectral resolution. With a pump irradiance of 1.12 W/cm^2 and a vapor cell temperature of 42^{o}C, the monochromator transmission and linewidth are ~17% and ~80 MHz, respectively.

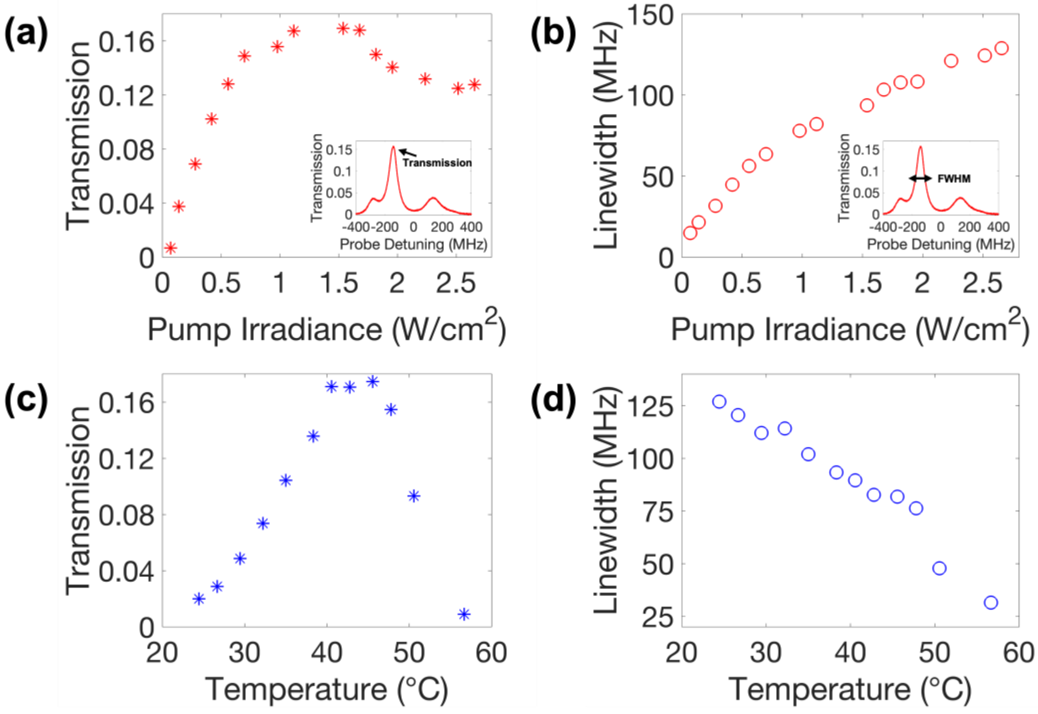

Figure 2.5. Characterization of LICD monochromator transmission and spectral resolution as a function of (a-b) pump irradiance and (c-d) vapor cell temperature. Insets for (a) and (b) show where the transmission FWHM are taken in the monochromator transmission spectrum.

2.2.2 Frequency tuning capabilities of the LICD atomic line monochromator

The frequency tuning capabilities of the monochromator, and thus the ability to build a spectrometer, are shown in Fig. 2.6. Tuning the pump frequency within the ^{87}Rb $5^2S_{1/2}$ ($F_g = 2$) Doppler broadened band allows us to probe and saturate different atomic velocity classes of the rubidium atoms in the vapor, thus shifting the transmission window, as shown in Fig. 2.6(a). The negative slope of the shift shows us that, when the pump is detuned to higher frequencies, the peak transmission shifts towards lower frequencies. The counter-detuning effect is due to the counterpropagating alignment of the lasers, which see atoms traveling at the same speed, but in different directions. Fig. 2.6(b) shows the transmission of the highest peak of the monochromator as a function of the pump detuning from the ^{87}Rb $5^2S_{1/2}$ ($F_g = 2$)$\rightarrow$$5^2P_{3/2}$ ($F_e = 3$) transition. A Gaussian fit (black trace in Fig. 2.6(b)) was used to estimate the FWHM of the envelope. The transmission envelope has a Gaussian FWHM of 509 MHz, which agrees with the Doppler width of Rb atoms [27,29,42]. Larger spectral ranges could be achieved with a different atomic vapor species. Potassium, for example, has a doppler-width of ~800 MHz at 770 nm [43-46]. To analyze different frequency ranges, the central frequency of the spectrum can be changed by tuning the incident beam frequency so that the spectrum falls inside the atomic vapor transmission window.

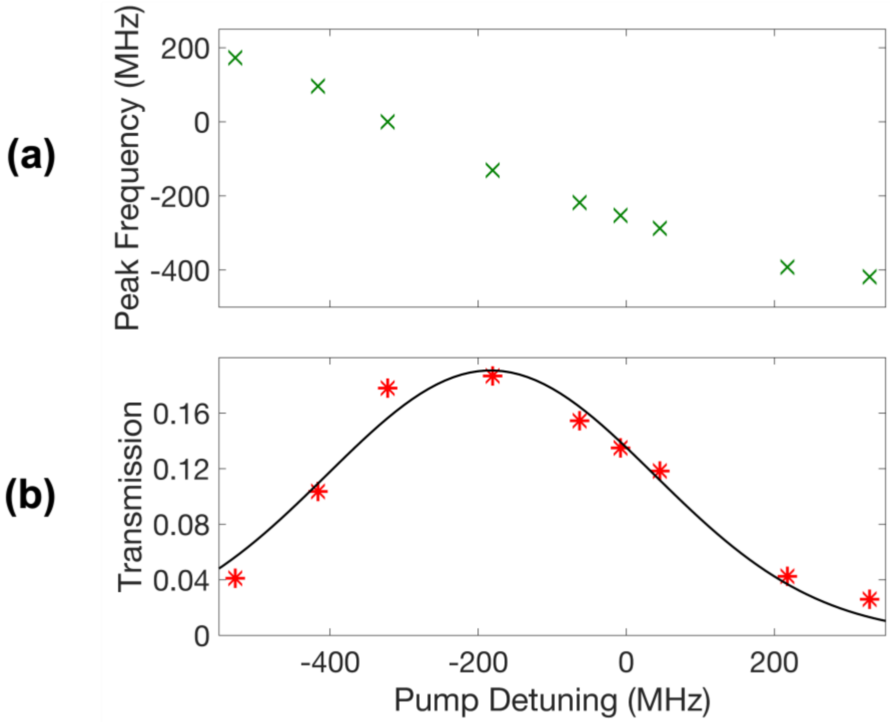

Figure 2.6. Frequency scanning capabilities of the monochromator. (a) Monochromator peak frequency detuning versus pump frequency detuning. (b) Monochromator transmission versus pump detuning (Gaussian fit is shown in black).

2.3 Imaging using the atomic line monochromator

2.3.1 Full-field spectroscopy

After characterizing transmission, resolution and tunability of the LICD monochromator, we demonstrated its capability to transmit an image, i.e., to provide simultaneous transmission of all the points in a field of view. To do so, the monochromator is designed so that the vapor cell is placed within a 4f system composed of the two 200 mm focal length lenses (L1 and L2 in Fig. 2.3). A USAF target (R3L1S4N, Thorlabs) was placed at the object plane *O* of L1, and the photodiode detector was replaced by an sCMOS camera (Andor, Zyla 4.2) at the front focal plane of the second lens.

Imaging results are shown in Fig. 2.7. Fig. 2.7(a) shows a test image of the USAF target element 5 of group 2, when the vapor cell is idle, i.e., the probe beam is off resonance, the pump beam is off, and the GT polarizers are in parallel configuration. When the polarizers are crossed, there is no image transmission, as seen in Fig. 2.7(b). Image transmission is achieved in Fig. 2.7(c) when the pump and probe beams are on resonance within the ^{87}Rb $5^2S_{1/2}$ (F_g = 2) absorption band. The pump beam was expanded to 1.69 mm in diameter and the irradiance was 1.12 W/cm^2. The probe laser irradiance was 11.2 mW/cm^2. Here, it was necessary to increase the probe power to overcome stray pump light reflected by the vapor cell window into the camera. Still, the transmission achieved in Fig. 2.7(c) was ~15.6%. When the beams are off resonance, instead, no image transmission was observed, as shown in Fig. 2.7(d).

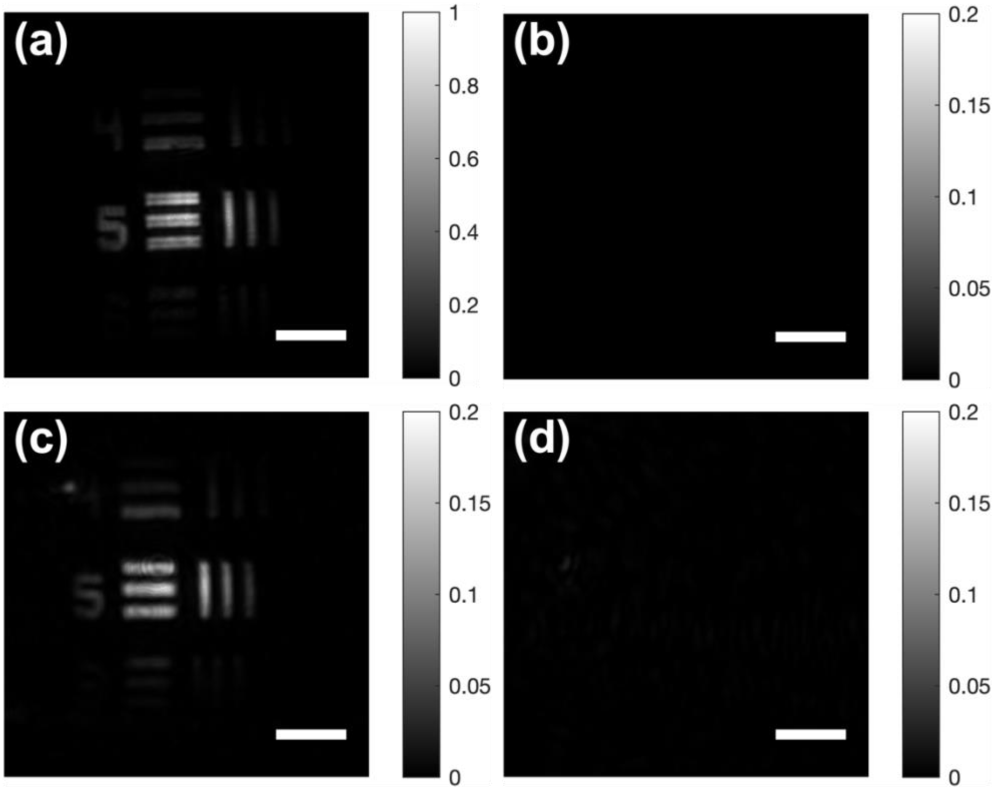

Figure 2.7. Image transmission of a USAF target through the LICD spectrometer (a) when the vapor cell is idle and polarizers are parallel, (b) when polarizers are crossed, (c) when the LICD monochromator is fully operational with pump and probe on resonance, and (d) when the probe beam is off resonance from the pump beam. Scale bars are 500 μm.

2.3.2 LICD atomic line monochromator effect on spatial resolution

Next, we established an operational definition of the effective diameter of the pump beam for the sake of imaging resolution. For this phenomenon, the critical physical property is the preparation of the ^{87}Rb atoms, thus the effective pump beam diameter is determined by having enough pump irradiance to saturate the atoms in a certain cross-sectional area. To confirm this idea experimentally, we kept the pump $1/e^2$ diameter at 1.35 mm and changed the pump irradiance while recording the spatial resolution. Indeed, we observed that changing the irradiance of the pump beam is equivalent to changing the diameter of a limiting pinhole in our 4f imaging system, as seen in Fig. 8(g). A pump irradiance of 0.42 W/cm^2 yields a resolution of 111.36 μm, 1.26 W/cm^2 yields a resolution of 88.5 μm, and 7.55 W/cm^2 yields a resolution of 78.7 μm. To estimate the effective cross-sectional area of the pump beam that sufficiently saturates the vapor, we used the definition of a Gaussian irradiance profile to calculate the effective diameter d_{eff} of a Gaussian laser beam

$$d_{eff} = 2\sqrt{\frac{-\omega^2 ln\left({I_{eff}}/{I_0}\right)}{2}}, \tag{2.1}$$

where ω is the $1/e^2$ diameter, I_{eff} is the irradiance of the Gaussian beam at d_{eff}, and I_0 is the peak irradiance at the center of the laser beam. By assuming that ω = 1.35mm and using I_{eff} as a free parameter, we used the Rayleigh criterion to fit the three estimated resolutions as a function of the pump peak irradiance shown in Fig. 8(g). Using the fit, we found that the cross-sectional area that predicts the experimental resolution was at I_{eff}=13.59 mW/cm^2, which is in good agreement with the experimental data (R^2 = 0.92). The back-calculated laser diameters at the 13.59 mW/cm^2 threshold were 1.76 mm for the 0.42 W/cm^2 pump irradiance, 2.02 mm for 1.26 W/cm^2, and 2.41 mm for 7.55 W/cm^2. The effective diameter of the limiting aperture of the imaging system are thus ~1.3-1.8 fold greater than the $1/e^2$ diameter of the pump beam.

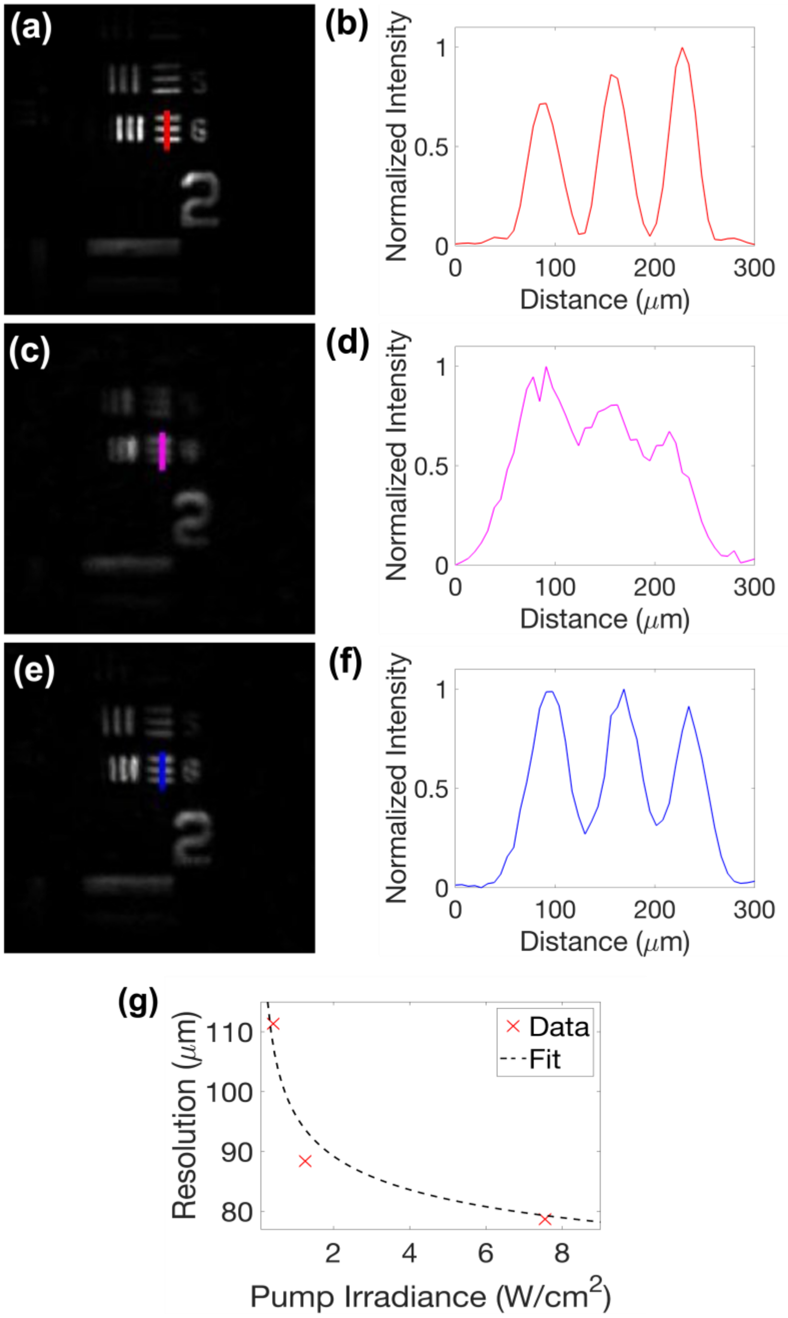

Figure 2.8. Image transmission of the USAF target at different pump diameters and irradiances. Test image and correspondent laser irradiance profile (a,b) when the monochromator is not operating, (c,d) when the monochromator is operating with 1.35 mm pump diameter,

and (e,f) 2.54 mm pump diameter. (g) Spatial resolution of our system versus the irradiance of the pump beam. The red crosses indicate experimental values taken with 0.42 W/cm^2, 1.26 W/cm^2, and 7.55 W/cm^2 pump irradiances when the laser 1/e^2 diameter is 1.35 mm. The black dashed line is the fit of the data using the Rayleigh criterion and Eq. (2.1), as explained in the text.

2.4 Conclusions

In summary, the LICD atomic line monochromator possesses ~17% transmission, ~80 MHz spectral resolution, and a scanning range limited to the doppler-width of Rb. We also proved that full-field spectroscopy is possible by transmitting an image of a USAF target when the image light is on resonance with the monochromator transmission band and image rejection when the image light is off resonance.

The LICD atomic line monochromator design from Fig. 2.3 suffers from two main drawbacks: the pump back reflection and the stringent scanning operation. The pump laser beam reflects from the window of the vapor cell and into the detector area. The pump back reflection creates a significant problem for Brillouin spectroscopy applications. The anti-reflection coating of the ^{87}Rb windows is ~0.5%, meaning that the back reflection is on the order of microwatts for an 8 mW pump laser power (1.12 W/cm^2 irradiance). Because the pump back reflection is orders of magnitude higher than the estimated Brillouin signal, the design is impractical for Brillouin applications. A potential solution to the pump back scattering is to implement a lock-in amplifier.

Lock-in amplifiers are used to detect a modulated signal that is drowned in significant background noise. For our purposes, we can modulate the pump background noise by using an acousto-optic modulator to vary the power of the pump laser. A lock-in amplifier can then be used to separate the modulated noise from the unmodulated probe signal. Lock-in amplifiers have been used to achieve shot-noise limited sensitivity in pump-probe schemes [47-50], however there are no easily available lock-in amplification approaches for 2D multiplexing.

Scanning the spectrometer frequency window by changing the pump frequency also presents challenges for Brillouin applications. The initial idea was to scan the probe beam within the ^{85}Rb (F=2) band, which is ~4.2 GHz away from the central frequency of the ^{87}Rb (F=2) band where the LICD spectrometer is operated. Locking the probe beam within the ^{85}Rb (F=2) band and using the probe to scan a sample would provide Brillouin photons, and the LICD transmission window could analyze Brillouin photons that have a ~4.2 GHz shift. Detuning the LICD spectrometer frequency window can only occur within the Doppler broadened band ^{87}Rb band, which is only ~500 MHz, so the Doppler-broadened window may be too narrow to study phenomena with a change in Brillouin shift that is greater than the 500 MHz. A possible solution is to, instead of locking the probe frequency and scanning the pump frequency, is to scan the probe frequency and lock the pump frequency. Locking the pump frequency fixes the monochromator central peak frequency, whereas scanning the probe beam essentially shifts the Brillouin spectrum through the transmission window. In this way, the dynamic range of the monochromator is limited to the scanning range of the laser (50 GHz in our case). The drawback to scanning the probe, however, is that scanning outside of the Doppler broadened bands prevents the use of atomic vapor cell notch filters that can reject Rayleigh scattered light. Locking the probe beam in the ^{85}Rb (F=2) band would mean that an ^{85}Rb atomic vapor cell notch filter could be added before the LICD setup to reject Rayleigh scattered light in that band, providing greater than 30 dB extinction [51-55].

Chapter 3

Brillouin spectroscopy via an atomic line monochromator

In this Chapter, we improve upon the LICD atomic line monochromator design from Chapter 2 for the first Brillouin measurements of this kind of device. The noise from the pump back-reflection presents a critical setback for Brillouin measurements. Operating both the pump and probe at the same wavelength prevents the usage of more traditional bandpass filters to be used to reject the pump back reflection and transmit the Brillouin signal.

The monochromator design from Chapter 2 relied on the pump frequency and the signal frequency being resonant with the same atomic transition and, as a result, operating at the same wavelengths. The purpose of Chapter 3 is to overcome the pump back reflection by using a pumping scheme that relies on the use of two different excited states of ^{87}Rb instead of one, unlike the ground state LICD spectrometer from Chapter 2. Using a pumping scheme that operates the pump laser at one frequency and transmits signal at another frequency allows for traditional bandpass filters to be used to transmit the signal light and reject the pump back reflections.

3.1 Ladder-type LICD atomic line monochromator design

3.1.1 Working principle

The atomic line monochromator presented in this Chapter is based on the laser induced circular dichroism (LICD) effect within a rubidium-87 (^{87}Rb) atomic vapor [28,29,56]. The pumping scheme for this monochromator is based on a ladder-type configuration: one for optical pumping and the other for signal transmission. A ladder-type atomic transition is a series of sequential transitions [57-60]. Figure 3.1 shows the pumping scheme of the new atomic line monochromator, which utilizes three ^{87}Rb orbitals: $5^2S_{1/2}$, $5^2P_{3/2}$, and $5^2D_{3/2}$ [61]. Each orbital is divided into different hyperfine levels, which consists of magnetic sublevels that can be accessed depending on the frequency and polarization of the incoming light.

Initially, a σ_+-circularly polarized pump laser, resonant with the $5^2S_{1/2}(F=2)\rightarrow 5^2P_{3/2}(F'=3)$ transition at $\omega_{\text{pump}} \cong 384.2304$ THz frequency and $\lambda_{\text{pump}} \cong 780.24$ nm wavelength, propagates inside of a pure ^{87}Rb vapor cell. The σ_+-polarized pump creates a +1 change in magnetic quantum number ($\Delta m = +1$) between the magnetic quantum numbers in the ground and excited states. The electrons spontaneously decay to the ground state following a $\Delta m = 0, \pm 1$ magnetic quantum number change [26]. Thus, the σ_+-polarized pump generates a cyclical effect between the ground state and the excited state magnetic sublevels until electrons occupy the $5^2S_{1/2}(F=2,\ m_F=+2)\rightarrow 5^2P_{3/2}(F'=3,\ m_{F'}=+3)$ transition. When the pump is powerful enough, the transition is saturated and the electron population densities in the $5^2S_{1/2}(F=2,\ m_F=+2)$ ground state and the $5^2P_{3/2}(F'=3,\ m_{F'}=+3)$ excited state are equal [34].

This optical pumping scheme prepares the vapor to exhibit circular dichroism for counter-propagating signal on resonance with the excited state transition $5^2P_{3/2}(F'=3) \rightarrow 5^2D_{3/2}(F''=3)$ at $\omega_0 \cong 386.3581$ THz frequency and $\lambda_0 \cong 775.94$ nm wavelength [56,59]. If the signal is π-polarized, and, therefore, composed of the two orthogonal circular polarization components, the circular polarization components of the signal will be absorbed differently by the atoms as governed by the selection rules for the magnetic quantum number. The left σ_--circular polarization component will be absorbed because there are magnetic sublevels in the $5^2D_{3/2}(F''=3)$ hyperfine state that are free to be occupied and obey the magnetic quantum number selection rule for σ_--polarized light (i.e., $\Delta m = -1$). Instead, the σ_+ component of the signal will not be absorbed because that transition is dipole forbidden. Thus, pumping at 780.24 nm has caused the vapor to be transparent for σ_+-polarized light at the $5^2P_{3/2}(F'=3) \rightarrow 5^2D_{3/2}(F''=3)$ resonance. We use this ladder-type pumping scheme to realize a high-resolution atomic line monochromator by inserting the optically pumped vapor in between two crossed linear polarizers. For the case of measuring Brillouin scattered light with a Brillouin shift $\pm \nu_B$, because the Brillouin shift has a linear dependance on the incident laser frequency, Brillouin photons will be transmitted through the atomic line monochromator when the incident laser has been detuned $\pm \nu_B$ away from the $5^2P_{3/2}(F'=3) \rightarrow 5^2D_{3/2}(F''=3)$ transition resonance. There will only be signal transmission through the atomic line monochromator at frequencies ω_0 and $\omega_0 \pm \nu_B$. In other words, tuning the incident laser frequency around the atomic line monochromator central frequency sweeps the Brillouin signal through the bandpass window, creating a high-resolution spectrometer.

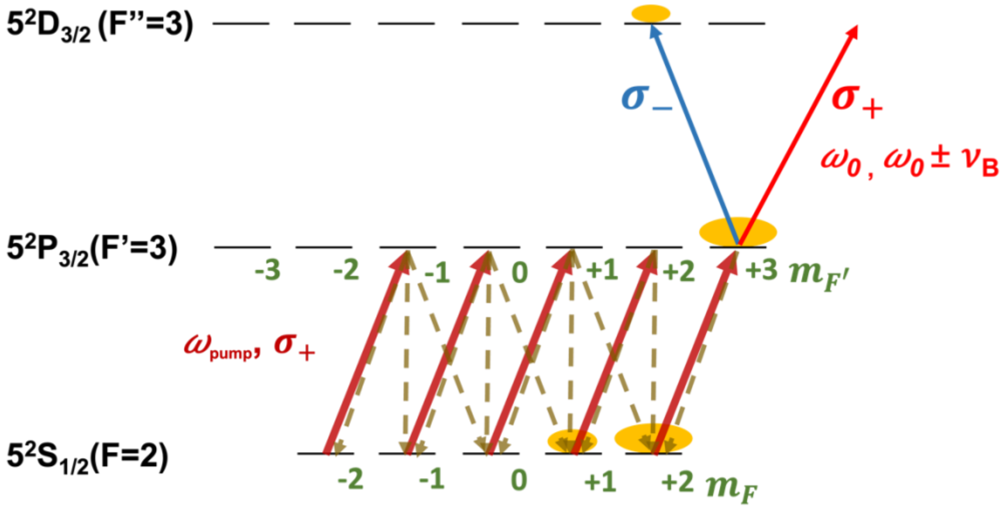

Figure 3.1. Ladder-type pumping scheme of the atomic line monochromator. The solid (dashed) arrows indicate absorption (decay) pathways. The pump changes the electron population density (yellow) in the ground state and excited state. The σ_+-polarized pump is resonant with the $5^2S_{1/2}$(F=2)→$5^2P_{3/2}$(F'=3) transition at a frequency ν_{pump} nm and the π-polarized signal light is on $5^2P_{3/2}$(F'=3)→$5^2D_{3/2}$(F''=3) transition at frequencies ω_0 and $\omega_0 \pm \nu_B$.

3.1.2 Experimental setup

The experimental setup is shown in Fig. 2. An epi-detection confocal microscope was built to collect Brillouin photons and combined with the atomic line monochromator for signal analysis. A tunable laser (DL pro, Toptica) acts as the incident laser and its central wavelength is near the ^{87}Rb $5^2P_{3/2}$(F'=3)→$5^2D_{3/2}$(F''=3) transition at 775.94 nm. The incident laser was split using a 50:50 (R:T) non-polarizing beam splitter cube (BS1), with one path leading to the microscope and the other path to a Fabry-Pérot interferometer (FPI, SA30-73, Thorlabs) for laser frequency calibration. When the laser frequency was scanned, the FPI resonance peaks were used to calibrate the incident laser frequency in GHz. In the microscope path, the incident laser passes through a polarizing beam splitter cube (PBS1) and a quarter-wave plate (QW1) before being focused by a microscope objective L1 (0.11 NA, 50 mm focal length) inside of a cuvette containing the sample. At the focus, the incident laser has a diameter of 4.3 μm. The same objective collects the Brillouin signal from the focal point. Due to QW1, the polarization of the collected signal changes and is reflected by PBS1 into a microscope objective (O1) and a polarization-maintaining fiber (PMF). The PMF serves as a confocal pinhole, restricting light collection to the focal plane, and sending the light to the atomic line monochromator for analysis. Using a saturated absorption spectroscopy module (CoSy, Toptica), the pump laser frequency (TA pro, Toptica) is locked to the ^{87}Rb $5^2S_{1/2}(F=2) \rightarrow 5^2P_{3/2}(F'=3)$ transition. The pump laser diameter out of the fiber collimator is 1.35 mm. The pump is σ_+-polarized using a quarter-wave plate (QW2), and a 10:90 (R:T) non-polarizing beam splitter (BS2) cube aligns the pump inside of a pure ^{87}Rb atomic vapor cell. From the PMF, the Brillouin signal is sent through the atomic line monochromator which is mainly composed of a pure ^{87}Rb atomic vapor cell and two crossed Glan-Taylor polarizers (GT1 and GT2; GT10-B Thorlabs). The signal is aligned to GT1 with a half-wave plate (HW1) and focused through the cell via a 4f system (L2 and L3, 200 mm focal length) to overlap with the counter-propagating pump beam inside the cell. The signal is finally transmitted through the polarizer GT2 (10^5:1 extinction ratio) which is crossed with GT1 and is focused onto an electron-multiplying charged-coupled device (EMCCD) camera (iXon Ultra897, Andor) using a 50 mm focal length lens (L4). A flip mirror is positioned before the final lens L4 so that it can reflect light into a photodiode detector (PDA36A2, Thorlabs). For simplicity of the data analysis, the monochromator characterization was completed with the photodiode detector instead of the EMCCD camera.

A feature of LICD atomic line monochromators is pump light back-reflected off the ^{87}Rb cell window into the detector. The pump-back-reflection is on the order of several microwatts of power and obstructs the optical path of the signal, which is orders of magnitude greater than spontaneous Brillouin scattered light due to a low scattering cross-section of 10^{-9} [62]. To address the pump-back-reflection, two bandpass filters F (Alluxa) were placed before the detector to provide 95% transmission at 775.94 nm and ~60 dB rejection at 780.24 nm. This is a significant improvement to the previous design of the LICD atomic line monochromator that utilized a single transition and therefore, could not use spectral filtering to block the pump background noise [18]. A spatial filter was also added after L3 and before GT2 to provide additional extinction of the pump background noise. The spatial filter was created using a 15 μm pinhole, an input lens O2 of 16.5mm focal length, and an output lens O3 of 18 mm focal length. The spatial filter provided an additional ~5 dB rejection of the back-reflected pump background noise while allowing ~88% transmission of the signal.

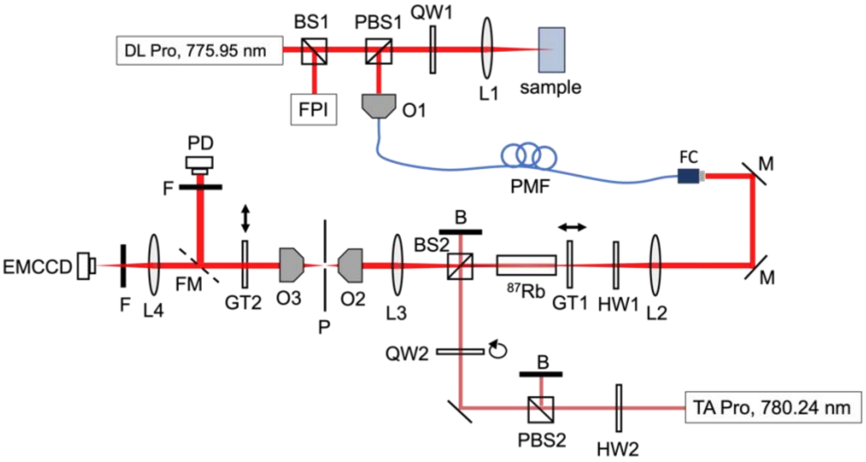

Figure 3.2. Setup schematic for the atomic line monochromator. L1, L2, L3,L4 lenses; PBS1, PBS2, polarizing beam splitter; BS1, BS2, non-polarizing beam splitter; QW1, QW2, quarter-wave plate; HW1, HW2, half-wave plate; FPI, Fabry-Pérot interferometer; P, pinhole; F, bandpass filter; PD, photodiode detector; O1,O2, O3, objective lens; B, beam block; M, mirror; GT1, GT2, Glan-Taylor polarizers; FM, flip mirror; PMF, polarization maintaining fiber; FC, fiber collimator.

3.2 Monochromator characterizations

3.2.1 Monochromator characteristic transmission band

To characterize the performances of the atomic line monochromator, the incident laser is fed directly to the monochromator to simulate the Brillouin signal. The flip mirror is up so that the signal intensity can be analyzed by the photodiode detector (Fig. 3.2). Figure 3.3 shows the characteristic transmission spectrum of our atomic line monochromator (red trace). The transmission is measured as the signal intensity after GT2 divided by the intensity of the signal before the ^{87}Rb cell. The signal power density is 0.36 mW/cm^2 before entering the ^{87}Rb cell and the pump power density is 3.35 W/cm^2 before entering the ^{87}Rb cell. The temperature of the ^{87}Rb cell is 55.6^{o}C. When the pump is blocked (black trace), the vapor is inert to 775.94 nm light and the laser is blocked by the polarizers, resulting in no signal transmission. When the pump is π-polarized (yellow trace), the vapor will not exhibit circular dichroism; as a result, the π-polarization of the signal is maintained and will be blocked by the second polarizer.

The monochromator transmission band consists of one peak split into two due to the high intensity of the pump, as governed by Aulter-Townes splitting [64-68]. At this pump power density, each peak has ~120 MHz linewidth and a peak-to-peak separation of 130 MHz as expected.

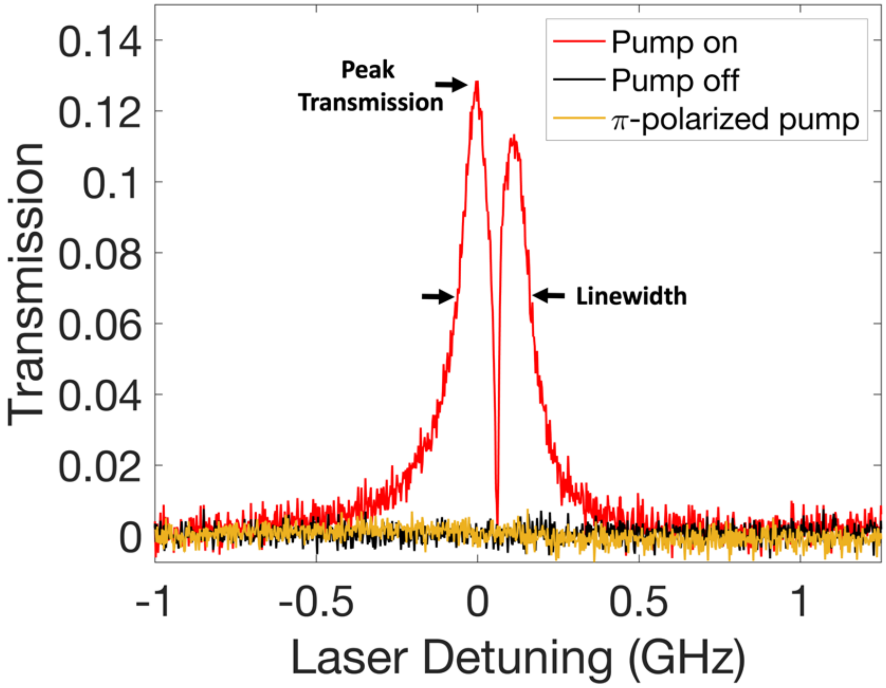

Figure 3.3. Monochromator transmission versus laser detuning. There is transmission when the pump is on and circularly polarized. There is no transmission when the circularly polarized pump is blocked (black trace) or π-polarized (yellow trace).

3.2.2 Transmission and linewidth characterizations

The transmission and the linewidth performances of the atomic line monochromator are characterized in Fig. 3.4, where the peak transmission is measured as the maximum intensity of the transmission spectrum and the linewidth is the full width at half maximum (FWHM) of the monochromator transmission band. The peak transmission and the linewidth are measures of the number of atoms that are saturated by the pump, which is highly dependent upon the pump power density and the temperature of the vapor. Figures 3.4(a,b) show the peak transmission and linewidth versus the pump power density when the vapor cell temperature is fixed at 55.6^{o}C. From Fig. 3.4(a), as the pump becomes more powerful the LICD effect in the atomic vapor becomes more pronounced, creating more transmission. The monochromator transmission eventually plateaus beyond ~3.3 W/cm^{2} because the pump has saturated the relevant transition. The linewidth increases as the pump power increases due to power broadening (Fig. 3.4(b)) [38,39]. Power broadening occurs when the pump intensity is so high that the electrons begin to oscillate more frequently between the ground and excited states, leading to a shorter transition lifetime and broader spectral peaks [26].

Figures 3.4(c,d) show the peak transmission and linewidth versus the ^{87}Rb cell temperature when the pump power density is fixed at 3.35 W/cm^{2}. From Fig. 3.4(c), the transmission increases as the temperature of the vapor increases because more atoms are interacting with both lasers as the temperature increases, improving the LICD effect. At temperatures exceeding 60^{o}C, the transmission decreases. The decrease in transmission is attributed to the pump being absorbed more at the cell entrance, saturating the vapor less while traveling through the vapor due to Beer's Law [41]. In Fig. 3.4(d), as the temperature increases the linewidth increases until becoming constant at ~56°C. The linewidth eventually decreases at 70°C, most likely because the contribution of the linewidth due to the Aulter-Townes splitting decreases significantly as the vapor absorbs the laser more. Overall, the monochromator can achieve ~13% transmission and ~230 MHz linewidth when the pump power density was 3.35 W/cm^2 and the temperature of the ^{87}Rb cell was 55.6°C.

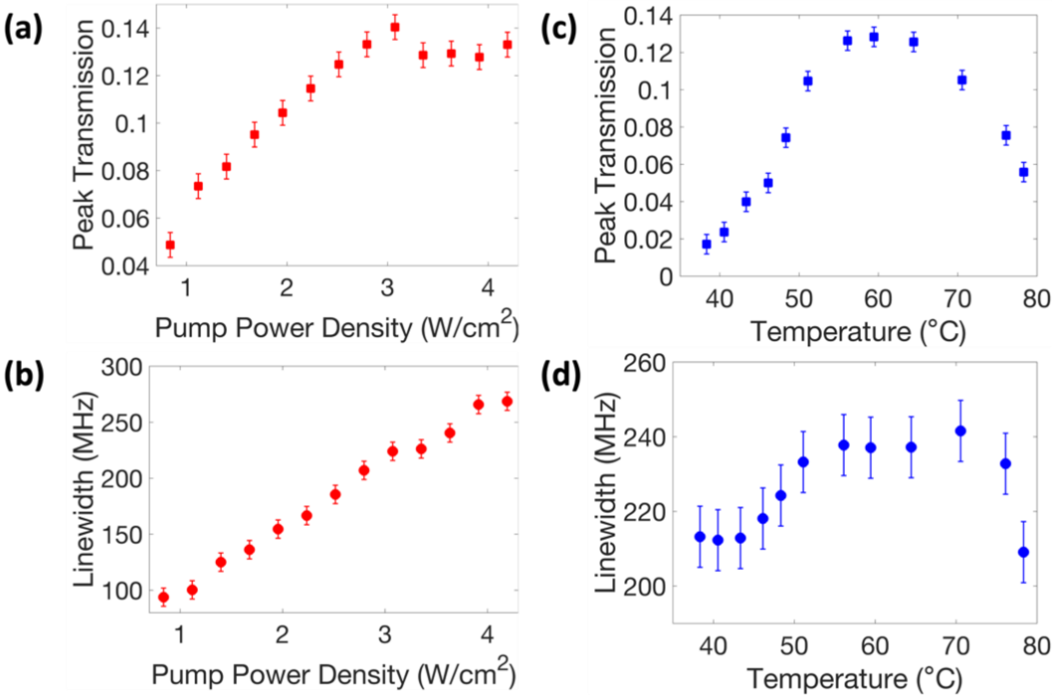

Figure 3.4. Characterization of the transmission and linewidth of the atomic line monochromator as a function of pump power density (a-b) and vapor cell temperature (c-d)

3.3 Brillouin measurements with the ladder-type atomic line monochromator

3.3.1 Brillouin measurements in clear liquid samples

After finding the optimal atomic line monochromator settings, the system was used to measure Brillouin spectra of liquids. Figure 3.5 shows Brillouin measurements of acetone and methanol using our Brillouin spectrometer, where the x-axis is the laser frequency detuning from the Rayleigh peak frequency. The laser power incident to the sample was 11.6 mW. The incident laser frequency was controlled by the diode laser cavity length, and the length of the cavity was adjusted by scanning a piezo motor. A voltage value was sent to the piezo motor using a custom LabView code, and the EMCCD camera acquires an image of the laser spot at each piezo voltage value. The acquisition time for each spectral datapoint was 200 ms with a 20 MHz step size. Each spectrum acquired consisted of 600 datapoints, leading to 2 minutes acquisition time per spectrum. The small step size was chosen to resolve the Autler-Townes splitting within the Rayleigh peak, however, the acquisition time for a single spectrum can be decreased by choosing a step size closer to the linewidth of the monochromator and taking fewer points. If we acquire a spectrum with only 40 spectral components, which is similar to the number of spectral components in a single VIPA free spectral range (i.e. VIPA finesse) [4], then the spectrum acquisition time for our spectrometer would be 8 seconds. The intensity of the signal at the focus was plotted as a function of the piezo voltage. The frequency axis of each scan was later calibrated from piezo voltage to GHz in post-processing using the FPI signal. Because the intensity of the signal at the Rayleigh frequency saturated the camera, the Brillouin shift was calculated as half the frequency difference between the Stokes and Anti-Stokes Brillouin peaks. The

Brillouin shifts of acetone and methanol were measured to be 4.062 GHz (5.8 MHz standard deviation) and 3.868 GHz (6.8 MHz standard deviation), respectively. These measurements agree with calculated Brillouin shifts using tabulated refractive index and sound velocity values [62,69].

As expected, the two characteristic peaks of the monochromator transmission band were reflected in the Rayleigh peak because the incident laser linewidth is ~300 kHz, orders of magnitude lower than the bandwidth of the monochromator. Instead, the linewidth of the monochromator is on the order of the natural Brillouin linewidths for acetone and methanol [62], leading to the measured linewidths of the samples being larger than their natural Brillouin linewidths. The measured linewidth for acetone and methanol were 395.31 MHz (8.75 MHz standard deviation) and 387.56 MHz (14.07 MHz standard deviation), respectively. Unlike the Rayleigh peak, the Autler-Townes splitting is not apparent in either Brillouin peaks because the natural Brillouin linewidths for acetone and methanol are larger than the 120 MHz Autler-Townes splitting. In the future, the natural Brillouin linewidth can be extracted by deconvolving the experimental data with the monochromator characteristic transmission band [70-74].

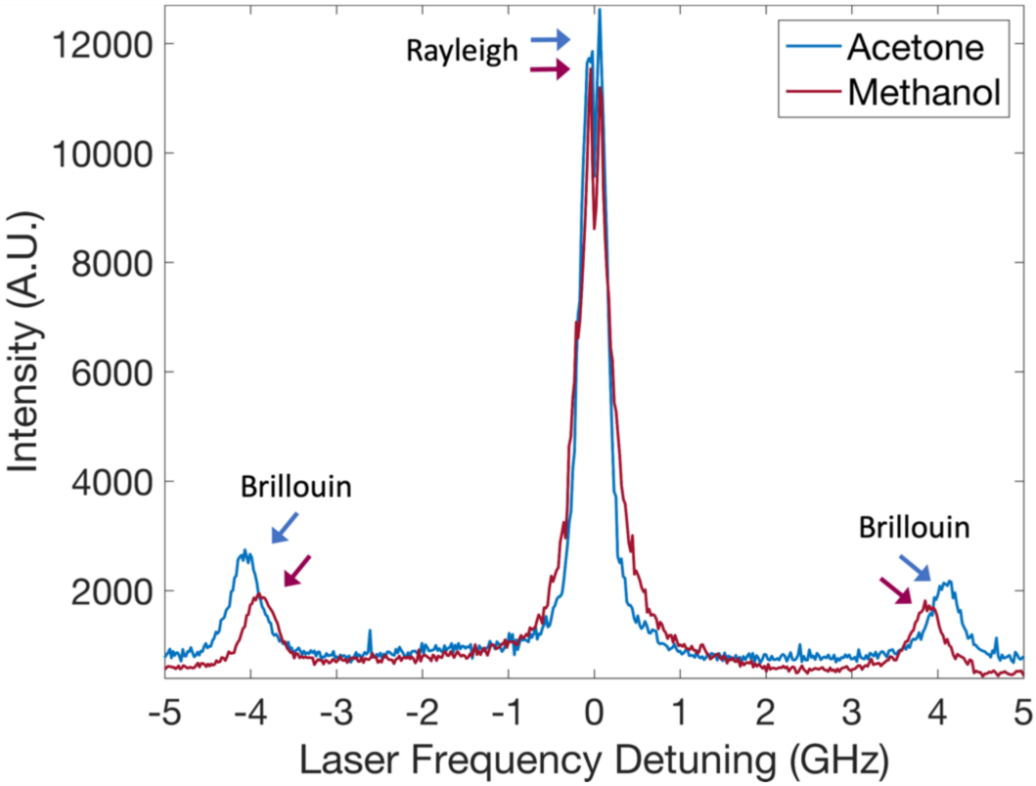

Figure 3.5. Brillouin scans of acetone and methanol using the atomic line monochromator.

3.3.2 Noise behaviors of the ladder-type atomic line monochromator

Although a considerable amount of the the pump-back-reflection off the ^{87}Rb vapor cell window is blocked by the bandpass filter (Fig. 3.2, F), the back-reflection constitutes a significant noise source in our spectrometer. The noise behavior of our Brillouin spectrometer was characterized in Fig. 3.6(a,b). First, the signal-to-background ratio (SBR) of the system was measured using an acetone sample (Fig. 3.6(a)). Examining the SBR of the system helps us understand if the noise source is system dependent or not. The laser power incident to the acetone sample was 16.3 mW and the pump power density is kept constant at 3.35 W/cm^2. The SBR was calculated as the ratio of the acetone Stokes peak's intensity to the average intensity of the background between the Stokes and Rayleigh peaks. Multiple scans were taken with varying image exposure times ranging from 20 to 400 ms. From 3.6(a), the SBR of the atomic line monochromator is constant at ~5.2 for different exposure times, indicating that the noise is system dependent.

The SBR measurement reveals a low signal strength compared to the pump-background noise, indicating inherent limitations in the detection sensitivity. To assess the device sensitivity further, we examined the signal-to-noise ratio (SNR) to estimate how far the system is from operating in the shot-noise limit where the system SNR would increase linearly with the square root of the number of photons measured. Figure 3.6(b) shows the signal-to-noise ratio (SNR) versus incident laser power to an acetone sample on a log-log scale. For each scan, the peak frequency of the incident laser was set to the frequency of the acetone Stokes peak, and 300 images of 200 ms exposure time were taken. The laser power incident to the sample varied between 1 and 12 mW for each measurement. In post-processing, 50 consecutive images were selected from the original set of 300 images to ensure the stability of the signal amidst potential variations, such as fluctuations in laser intensity and laser frequency drift for the pump laser and the laser incident to the sample. The SNR was calculated as the ratio between the mean intensity of the 50 measurements and the variance in intensity of the 50 measurements. From 1 to 1.7 mW of incident laser power, the SNR is constant because the signal was at the noise floor of the pump background. At incident laser powers greater than 2 mW, the SNR increases. The dashed black line is a linear fit to the SNR data past the noise floor, where the slope of the line is 0.3975. If the system were operating in the shot-noise limited regime the slope of the fit would be .5. By using more incident laser power the signal would eventually increase above the noise floor enough to where measurements could be conducted in the shot-noise limit. However, due to system constraints, we could not increase the incident laser power further. Nevertheless, by performing a power law fitting with the data from Fig. 3.6(b), we were able to extrapolate the behavior of the system to higher incident power levels. From the extrapolated curve, we estimate that the system reaches the shot-noise limited behavior at ~37 mW incident power.

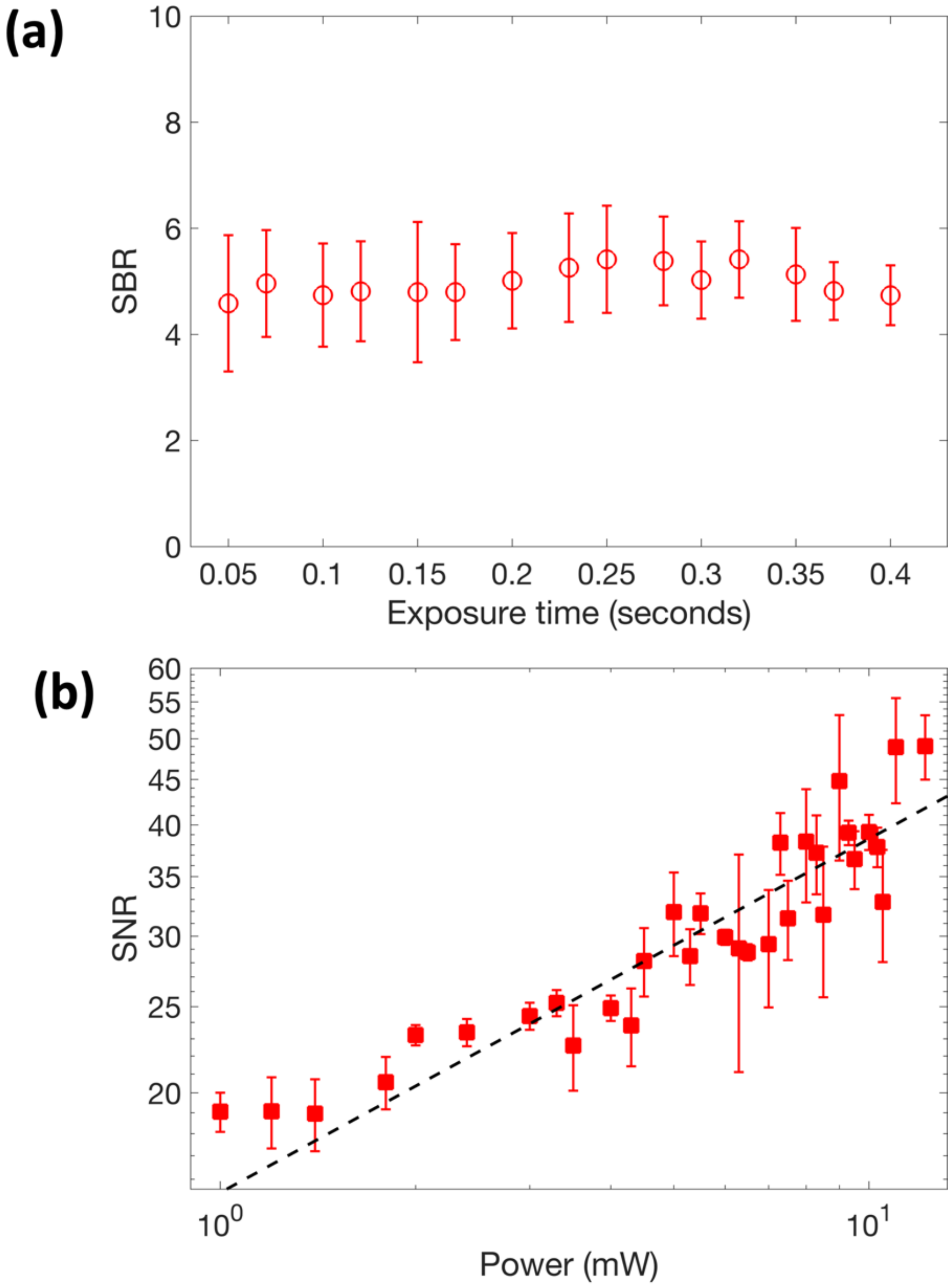

Figure 3.6. Atomic line monochromator noise characterizations. (a) Signal-to-background ratio of acetone Brillouin measurements as a function of camera exposure time. (b) Signal-to-noise ratio of the acetone Brillouin measurements as a function of power incident to the sample on a log-log scale.

3.4 Conclusions

In summary, we have built the first atomic line monochromator for practical measurements of Brillouin scattering in clear liquid samples. The transmission and linewidth of the atomic line monochromator was ~13% and ~230 MHz, respectively. Using a ladder-type atomic transition that allows us to operate the pump laser and the signal at different frequencies permits the use of bandpass filters that significantly decreased the pump-background noise (~60 dB), allowing us to demonstrate the spectrometer proof-of-principle by measuring spontaneous Brillouin scattering in clear liquids.

Although the pump-background rejection was sufficient for Brillouin measurements, a feature of the monochromator design in Chapter 3 is that there is still light from the pump bleeding through the filter and into the camera. Currently, a spatial filter is used to reject some of the pump light bleeding through the bandpass filter, but a spatial filter with a circular pinhole limits the system to point-scan spectral analysis and makes future imaging applications difficult. More than likely, amplified spontaneous emission (ASE) from the diode of the laser is bleeding through the transmission window of the bandpass filter [75-78]. To reject ASE, Bragg gratings can be added to further clean the laser line so that the noise floor of the laser can be decreased by 15dB, which may even lead to shot-noise limited measurements of water. Another solution for addressing the ASE would be to use a different pumping scheme that has a larger separation between the pump laser frequency and the signal frequency. The intensity of ASE is greater at the wings of the laser line, so having a large separation between the two laser frequencies would mean that there is less ASE to reject.

The extinction of the ladder-type atomic line monochromator setup is limited to the extinction of the crossed polarizers, which is 50 dB. Typically, >70 dB extinction is preferred when measuring the Brillouin photons of biological samples [4,7,9,10,79], but this metric is based on the 180^{o} detection systems where significant background can arise from reflections in the system that are reflected into the spectrometer [3,80]. Even though it was proposed that an atomic vapor cell notch filter can add additional extinction to an LICD setup in Chapter 2, this approach is not easily achievable for the ladder-type pumping scheme because to absorb the ~775.94 nm Rayleigh line an ^{85}Rb notch filter would have to make the 5S-5P transition before being able to absorb ~776 nm Rayleigh light.

Chapter 4

Full-field Brillouin microscopy using a V-type atomic line monochromator

This Chapter introduces a novel Brillouin microscope technique that is capable of pixel multiplexing using an atomic line monochromator for spectral analysis. The ladder-type atomic line Brillouin spectrometer developed in Chapter 3 is the first practical implementation of a Brillouin spectrometer based completely on atomic vapors. However, the significant amount of pump background noise required the addition of a spatial filter, limiting the ladder-type atomic line monochromator to single-pixel Brillouin signal acquisition. The purpose of this Chapter is to create an atomic line monochromator with sufficient noise rejection of the pump background noise without the requirement of a spatial filter. The atomic line monochromator developed in this Chapter is based on a new pump-probe scheme that suffers from less pump background noise than previous implementations of the device. We characterize the performances of this new atomic line monochromator, as well as combine the new monochromator with line-illumination for one-dimensional (1-D) multiplexing of Brillouin signal in clear liquids.

4.1 V-type LICD atomic line monochromator design and characterizations

The monochromator described in this Chapter utilizes a V-type pump-probe scheme. For V-type pump-probe schemes, the pump and the probe are resonant with two different atomic transitions that share the same ground state [81-84]. The so-called V-type monochromator presented here uses a pump that is resonant with the D_1 ^{87}Rb $5^2S_{1/2}(F_g = 2)\rightarrow 5^2P_{1/2}(F_e = 2)$ transition at 794.98 nm and a probe that is resonant with the D_2 ^{87}Rb $5^2S_{1/2}(F_g = 2)\rightarrow 5^2P_{3/2}(F'_e = 3)$ transition at 780.24 nm.

4.1.1 Working principle

Consider the hyperfine structure of the ^{87}Rb $5^2S_{1/2}\rightarrow 5^2P_{1/2}$ D_1 line. Figure 4.1(a) shows the allowable transitions of the ^{87}Rb $5^2S_{1/2}(F_g = 2)$ hyperfine ground state to the ^{87}Rb $5^2P_{1/2}(F_e = 1$ and $2)$ hyperfine excited states, as well as the cross-over (CO) transition that occurs between the two hyperfine resonances. Figure 4.1(b) shows the Doppler-free absorption spectrum of the D_1 ^{87}Rb $5^2S_{1/2}(F_g = 2)\rightarrow 5^2P_{1/2}(F_e = 1$ and $2)$ transitions and the CO peak acquired using a CoSy unit.

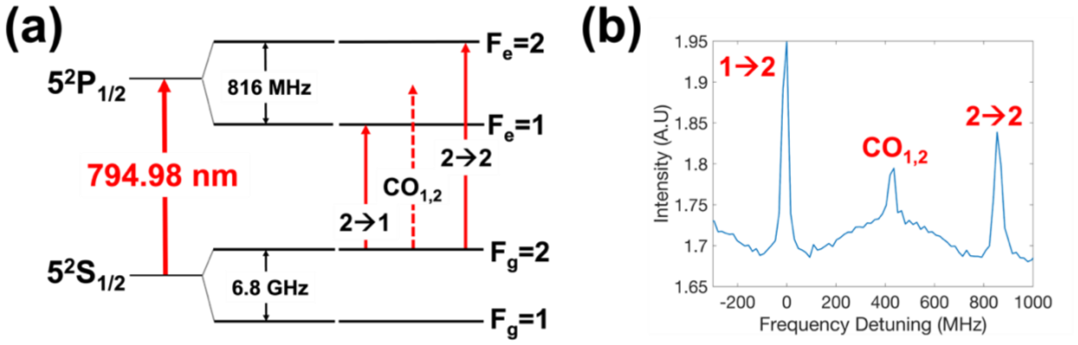

Figure 4.1. Hyperfine transitions of the ^{87}Rb D_1 line. (a) Transition schematic of the D_1 ^{87}Rb $5^2S_{1/2}(F_g = 2)\rightarrow 5^2P_{1/2}$ $(F_e = 1$ and $2)$ and the crossover peak (dashed arrow); (b)

Doppler-free spectrum of the D_1 ^{87}Rb $5^2S_{1/2}(F_g = 2) \rightarrow 5^2P_{1/2}$ (F_e = 1 and 2) and the crossover peak.

The pumping scheme is shown in Fig. 4.2(a). First, the pump laser is σ_+-polarized and propagates inside a pure ^{87}Rb atomic vapor cell. The σ_+-polarization of the pump creates a +1 change in magnetic quantum number ($\Delta m = +1$) between the magnetic quantum numbers in the $5^2S_{1/2}(F_g = 2)$ ground state and the $5^2P_{1/2}(F_e = 2)$ excited state. The electrons spontaneously decay to the ground state following a $\Delta m = 0, \pm 1$ magnetic quantum number change [26]. When the pump is powerful enough, a high electron population density will occur in the $5^2S_{1/2}(F_g = 2, m_{Fg} = +2)$ magnetic sublevel due to the $\Delta m = +1, 0$ spontaneous decay channels from the $5^2P_{1/2}(F_e = 2, m_{Fe} = +1, +2)$ magnetic sublevels in the excited state.

When the pump is resonant with the D_1 ^{87}Rb $5^2S_{1/2}(F_g = 2) \rightarrow 5^2P_{1/2}(F_e = 2)$ transition at 794.98 nm, the pump has prepared the atomic vapor to experience circular dichroism near the D_2 ^{87}Rb $5^2S_{1/2}(F_g = 2) \rightarrow 5^2P_{3/2}(F'_e = 3)$ transition at 780.24 nm. For the case of π-polarized probe light, the two orthogonal circular polarization components will be absorbed by two different magnetic sublevel transitions (Fig. 4.2(b)). The σ_+-component of the probe light will be resonant with the $5^2S_{1/2}(F_g = 2, m_{Fg} = +2) \rightarrow 5^2P_{3/2}(F'_e = 3, m_{F'e} = +3)$, while the $\sigma\_$-component will be resonant with the $5^2S_{1/2}(F_g = 2, m_{Fg} = +2) \rightarrow 5^2P_{3/2}(F'_e = 3, m_{F'e} = +1)$ transition. The two orthogonal circular polarization components of the probe will be absorbed differently due to the distinct transition probabilities between the atomic transitions that they interact with. The probability of absorption describes the strength of interaction between atoms and resonant optical radiation [85]. Atomic transition probabilities are proportional to the Clebsch-Gordan coefficient of a transition, which is the amplitude of the angular momentum coupling between the ground state and the excited state of an atomic transition [36]. The Clebsch-Gordan coefficient for the $5^2S_{1/2}(F_g = 2, m_{Fg} = +2) \rightarrow 5^2P_{3/2}(F'_e = 3, m_{F'e} = +3)$ transition is $\sqrt{1/2}$, while the Clebsch-Gordan coefficient for the $5^2S_{1/2}(F_g = 2, m_{Fg} = +2) \rightarrow 5^2P_{3/2}(F'_e = 3, m_{F'e} = +1)$ transition is $\sqrt{1/30}$ [28]. In other words, the σ_+-component of the probe has an absorption probability that is ~3.88 stronger than that of the $\sigma\_$-component. The V-type pump-probe scheme has prepared the atomic vapor to experience circular dichroism near the $5^2S_{1/2}(F_g = 2) \rightarrow 5^2P_{3/2}(F'_e = 3)$, shifting the polarization of incoming π-polarized light and creating transmission past a crossed linear polarizer downstream.

Brillouin spectroscopy can be implemented using the V-type atomic line monochromator by using a tunable laser source. The Brillouin photons of frequency shift ν_B, acting as the probe light, will be generated with an incident laser that is near resonance with the D_2 ^{87}Rb $5^2S_{1/2}(F_g = 2) \rightarrow 5^2P_{3/2}(F'_e = 3)$ transition at 780.24 nm. When the incident laser is detuned by a frequency ν_B (i.e., 780.24 nm $\pm \nu_B$), the Brillouin photons will be on resonance with the V-type atomic line monochromator bandpass window. Much like the ladder-type pump-probe scheme described in Chapter 3, the V-type pump-probe scheme uses two different laser wavelengths, creating a way for spectral filters to reject the pump-background noise. However, the wavelength difference between the pump and probe in Chapter 3 was ~4 nm, which necessitated ultra-narrow bandpass filters for rejecting the pump background noise and high-quality Bragg gratings for spectral filtering of the laser. The V-type pump-probe scheme used for this Chapter has a ~15 nm difference between pump and probe laser wavelengths, leading to more commercially available filters with higher spectral extinction of the pump background light. Also, the spectral filtering of the pump laser is more simplified because laser noise such as ASE decreases further away from the laser line frequency [86].

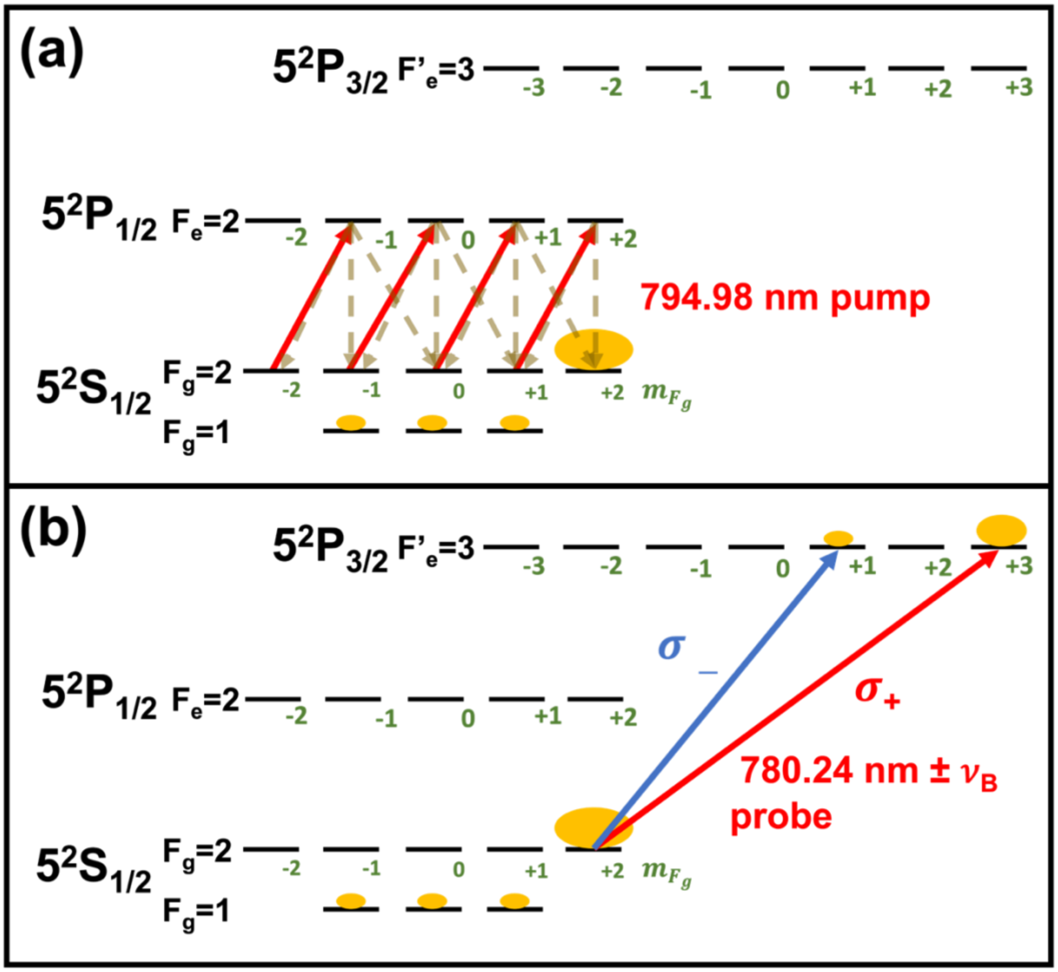

Figure 4.2. The atomic line monochromator V-type pump-probe scheme. (a) The σ+-polarized pump is resonant with the $5^2S_{1/2}$(F=2)→$5^2P_{1/2}$(F$_e$=2) transition at 794.98 nm, creating a population of electrons in the $5^2S_{1/2}$(F=2, m_{Fg} =+2) magnetic sublevel. (b) The π-polarized probe is resonant with the $5^2S_{1/2}$(F=2)→$5^2P_{3/2}$(F'$_e$=3) transition at

780.24 nm. The solid arrows depict absorption channels, and the dashed arrows depict decay pathways.

4.1.2 Experimental setup

The full-field Brillouin microscope experimental setup is shown in Fig. 4.3. The microscope is split between the illumination arm and the detection arm. In the illumination arm, a tunable wavelength diode laser (DL pro, Toptica) serves as the light source, operating at a central wavelength of 780.24 nm. The laser wavelength can be adjusted within the D_2 lines of ^{87}Rb and ^{85}Rb using a CoSy module. The laser line is spectrally cleaned using two ultra-narrow reflective Bragg gratings (BP-780, OptiGrate), each providing ~15dB rejection laser line noise. The laser is expanded to a 9.5 mm diameter using a telescope before being focused into a sample cuvette by a microscope objective (4X/0.1 NA, Olympus), generating a tightly focused line beam of Brillouin photons that acts as the probe light for the V-type pump-probe scheme from Fig. 4.2(b).

The detection arm is a 1.4X magnification imaging system set 90^{o} to the illumination arm to allow for multiplexed Brillouin spectroscopy, where the V-type atomic line monochromator is in the infinite space of the imaging system. The laser beam is imaged onto a slit with two objective lenses (20X/0.4 NA, 4X/0.1 NA, Olympus). The light is relayed using a 400 mm focal length tube lens and the final image is created using a spherical lens (400 mm focal length). The V-type atomic line monochromator consists of a pure ^{87}Rb sandwiched between two crossed Glan-Taylor linear polarizers (10^5:1 extinction ratio, GT-10B, Thorlabs) and a pump laser. The pump laser (TA pro, Toptica) central wavelength is 794.95 nm and can locked at different resonances with the D_1 lines ^{87}Rb using a CoSy module. The pump laser beam diameter is expanded to ~4.05 mm using a telescope. The pump laser line is spectrally cleaned using a long-pass filter (RET792lp, Chroma), providing 60 dB spectral extinction of laser line noise. The pump laser is σ_+-polarized using a quarter-wave plate and is aligned to counter-propagate with the probe signal inside of the ^{87}Rb cell using a short-pass dichroic mirror (DMSP805, Thorlabs). An EMCCD (iXon, Andor) camera is placed at the focus of the imaging lens for the detection of the Brillouin signal. Two spectral filters (F3, FBH05780-10, Thorlabs) are placed before the camera, each possessing a transmission of 95% at 780.24 nm probe signal and ~60dB spectral extinction at 794.95 nm pump background noise.

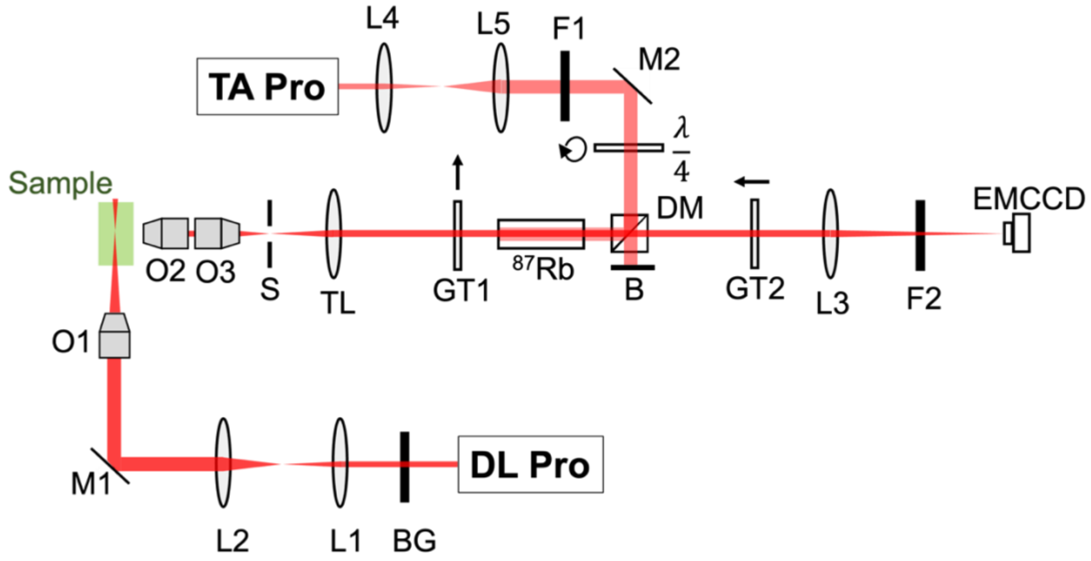

Figure 4.3. Setup schematic for the full-field Brillouin microscope: B, beam block; BG, Bragg gratings; F1, F2, spectral filters; GT1, GT2, Glan-Taylor polarizers; L1, L2,

L3, L4, L5, spherical lenses; M1, M2, mirrors; O1, O2, O3, objective lenses; S, slit; TL, tube lens; $\lambda/4$, quarter-wave plate.

4.1.3 Monochromator transmission and spectral resolution

To characterize the transmission and linewidth performances of the V-type atomic line monochromator, a separate incident laser source (DL pro, Toptica) is used to the probe signal, and the EMCCD is replaced with a photodiode detector (PDA36A2, Thorlabs) for detection. The characteristic PSF of the V-type atomic line monochromator is shown in Fig. 4.4 when the probe power density before entering the ^{87}Rb vapor cell is 1.03 mW/cm^2, the pump power density before entering the cell is .9 W/cm^2, and the temperature of the atomic vapor cell is 51.7^{o}C. The pump laser frequency is locked to the D_1 ^{87}Rb $5^2S_{1/2}(F_g = 2) \rightarrow 5^2P_{1/2}(F_e = 2)$ transition at 794.98 nm and the probe laser is scanned near the D_2 ^{87}Rb $5^2S_{1/2}(F_g = 2) \rightarrow 5^2P_{3/2}(F'_e = 3)$ transition at 780.24 nm. The frequency axis is calibrated from the laser piezo voltage using the Doppler-free absorption spectrum acquired with the CoSy module, where the zero point of the axis is the ^{87}Rb $5^2S_{1/2}(F_g = 2) \rightarrow 5^2P_{3/2}(F'_e = 3)$ frequency. The PSF has two noticeable peaks: one peak on resonance on resonance with the ^{87}Rb $5^2S_{1/2}(F_g = 2) \rightarrow 5^2P_{3/2}(F'_e = 3)$ transition and another less intense peak ~500 MHz away. The monochromator transmission is defined as the maximum intensity of the peak at the ^{87}Rb $5^2S_{1/2}(F_g = 2) \rightarrow 5^2P_{3/2}(F'_e = 3)$ frequency and the linewidth of the monochromator is the FWHM of the same peak.

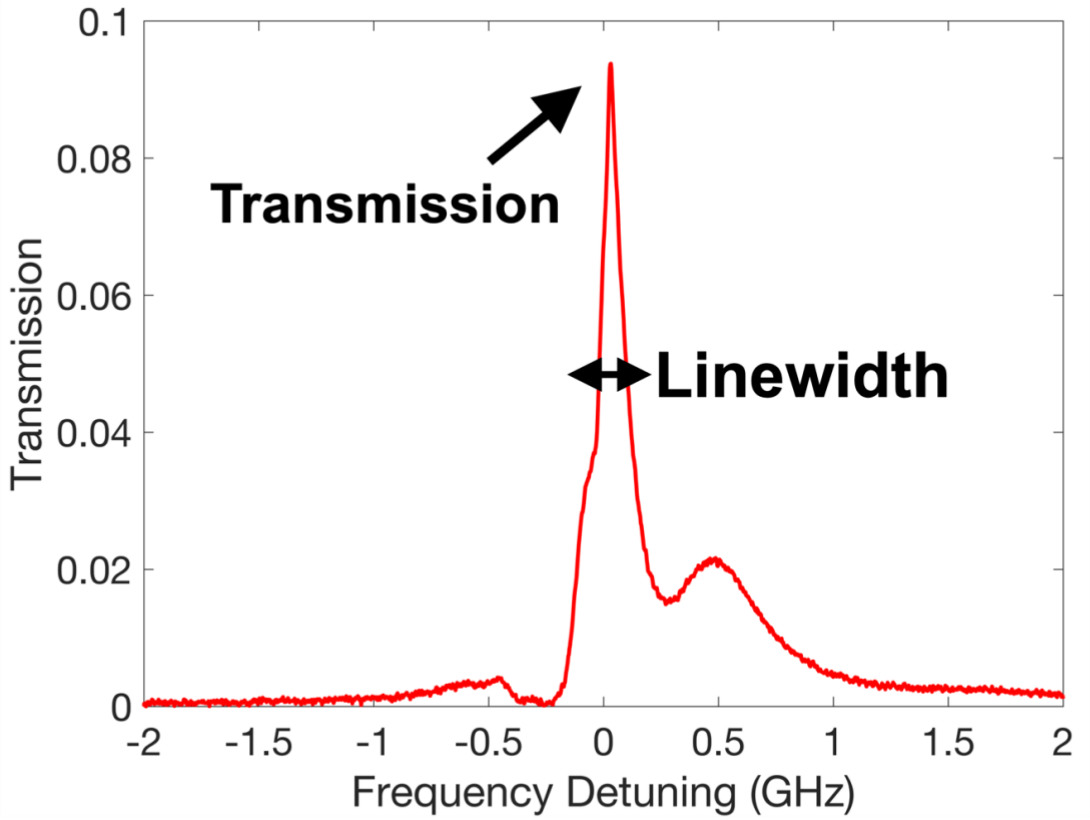

Figure 4.4. Characteristic PSF of the V-type atomic line monochromator.

The behavior of the V-type atomic line monochromator with variable pump power density was investigated. Fig. 4.5(a) shows the transmission of the V-type atomic line monochromator as a function of pump power density. The probe power density is 1.03 mW/cm^2 before entering the atomic vapor cell and the vapor cell temperature is maintained at 51.7^{o}C. As the pump power density increases, the monochromator transmission increases because the pump has prepared more electrons to the D_1 $5^2P_{1/2}(F_g = 2, m_{Fg} = +2)$ magnetic sublevel to be absorbed by the probe laser. The transmission eventually saturates at higher pump powers, however, saturation for our V-type pump-probe scheme is not the same as the saturation of a two-level atom.

Because the optically-pumped transition is an “open” transition [87-89], meaning that the electrons are being optically pumped to a magnetic sublevel that is not a part of the optical pumping process, saturation here means that further increases in pump intensity yield diminishing returns due to the balances of the relaxation processes to the $5^2P_{1/2}(F_g = 2, m_{Fg} = +2)$ magnetic sublevel. The linewidth behavior as a function of the pump power density was also investigated (Fig. 4.5(b)). The linewidth of the V-type atomic line monochromator increases as the pump power density increases due to the power broadening that the pump laser creates at the D_1 ^{87}Rb $5^2S_{1/2}(F_g = 2) \rightarrow 5^2P_{1/2}(F_e = 2)$ transition. Overall, when the pump power density before entering the cell is .9 W/cm^2 and the temperature of the atomic vapor cell is 51.7^{o}C, the V-type atomic line monochromator possesses a transmission of 9.4% and a linewidth of 127 MHz.

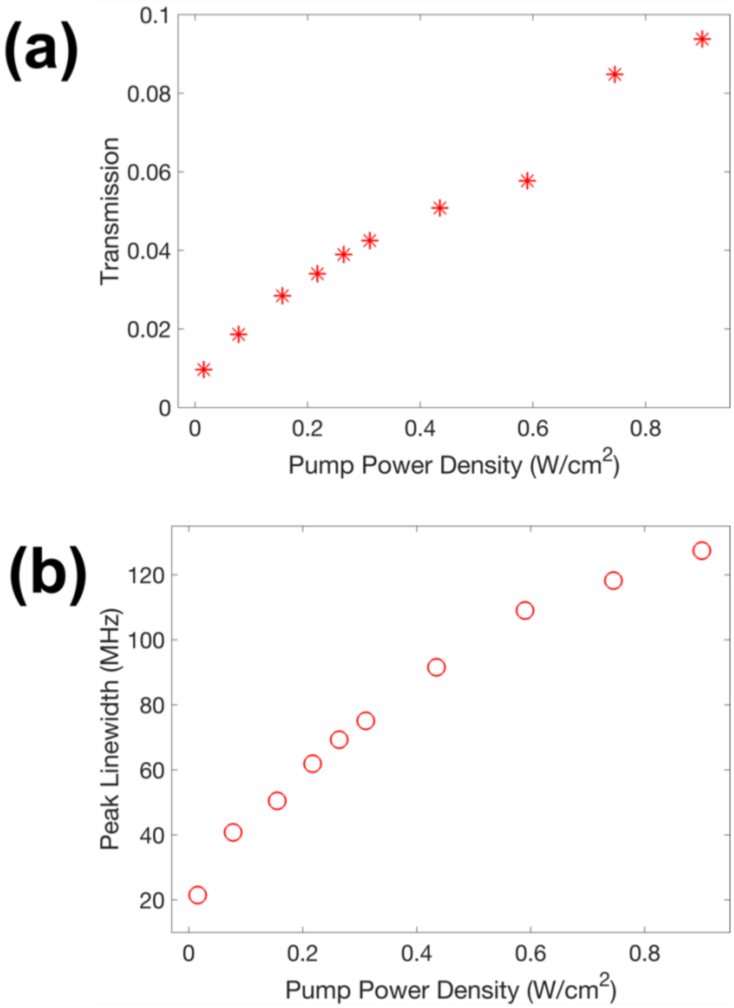

Figure 4.5. Pump power density characterizations of the V-type atomic line monochromator characterizations. (a) Monochromator transmission as a function of pump power density. (b) Monochromator linewidth as a function of pump power density

4.2 Full-field Brillouin microscopy

4.2.1 Full-field Brillouin imaging in clear liquid samples

1-D multiplexed Brillouin imaging was demonstrated in a methanol sample using the full-field Brillouin microscope. The incident laser power at the sample was 335 mW, the V-type atomic line monochromator pump power density was .9 W/cm^2, and the vapor cell temperature was 51.7°C. The image acquisition time for the EMCCD camera was 500 ms. The incident laser frequency is changed to different frequencies near the D_2 lines of ^{87}Rb and ^{85}Rb, while the pump laser frequency is locked at the D_1 ^{87}Rb $5^2S_{1/2}(F_g = 2) \rightarrow 5^2P_{1/2}(F_e = 2)$ transition. Figure 4.6(a) shows a full-field Brillouin image when the frequency of the incident laser is on resonance with the ^{87}Rb $5^2S_{1/2}(F_g = 2) \rightarrow 5^2P_{3/2}(F'_e = 3)$ transition. The laser line is barely noticeable due to a significant amount of background noise that arises from reflections from the optics in the system. In Fig. 4.6(b), the incident laser frequency is detuned 1 GHz away from the ^{87}Rb $5^2S_{1/2}(F_g = 2) \rightarrow 5^2P_{3/2}(F'_e = 3)$ transition within the ^{85}Rb ($F_g = 3$) band. Image transmission is no longer possible in this case because the incident laser frequency is not generating photons that are on resonance with the V-type atomic line monochromator bandpass. As a result, the probe polarization is not flipped, and the image is blocked by the output polarizer. Methanol Brillouin photons were collected using the full-field Brillouin microscope when the incident laser frequency was detuned ~2.44 GHz away from the ^{87}Rb $5^2S_{1/2}(F_g = 2) \rightarrow 5^2P_{3/2}(F'_e = 3)$ transition (Fig. 4.6(c)). Detuning the incident laser frequency by the Brillouin shift of methanol makes it so that the Brillouin photons are on resonance with the V-type atomic line monochromator bandpass, creating transmission. The background noise visible in Fig. 4.6(a) is not visible in Fig. 4.6(c) because the noise is not the same frequency as the Brillouin photons and thus not on resonance with atomic line monochromator bandpass, further validating that we are measuring Brillouin scattered photons.

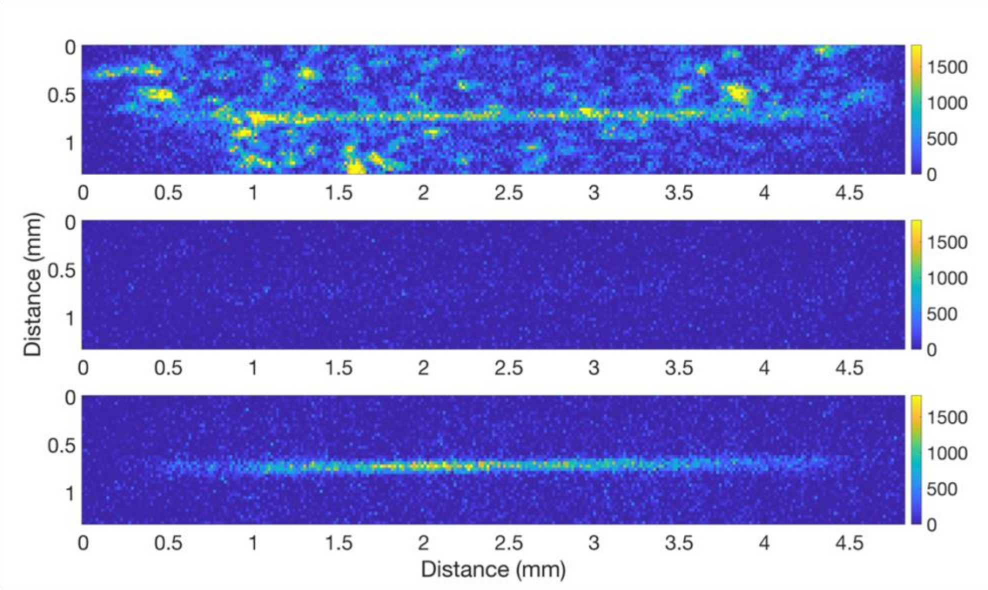

Figure 4.6. Demonstration of full-field Brillouin imaging with a methanol sample. (a) Full-field Brillouin image when the incident laser frequency is on resonance with the $5^2S_{1/2}(F_g = 2, m_{Fg} = +2) \rightarrow 5^2P_{3/2}(F'_e = 3, m_{F'e} = +3)$ transition. (b) Full-field Brillouin image when the incident laser frequency is detuned ~1 GHz away from the $5^2S_{1/2}(F_g = 2, m_{Fg} = +2) \rightarrow 5^2P_{3/2}(F'_e = 3, m_{F'e} = +3)$ transition. (c) Full-field Brillouin image of when the incident laser is detuned near the Brillouin frequency of methanol.

The Brillouin spectra for methanol and acetone were constructed using the full-field Brillouin microscope (Fig. 4.7), where the incident laser intensity at the sample was 335 mW and the V-type atomic line monochromator was fully operational. The Brillouin spectra are constructed by plotting the mean intensity across the Brillouin line signal at different incident laser frequencies. The incident laser frequency was coarsely adjusted by changing the laser cavity piezo. For each piezo voltage, an image was taken with the full-field Brillouin microscope at 200 ms exposure time. The incident laser piezo voltage values for each image were converted in units of GHz during post-processing using the Doppler-free absorption spectrum generated by the CoSy module. The zero point of the x-axis is the Rayleigh frequency, which is also when the incident laser frequency is on resonance with the ^{87}Rb $5^2S_{1/2}(F_g = 2) \rightarrow 5^2P_{3/2}(F'_e = 3)$ transition. The Brillouin shift of methanol was measured to be 2.44 GHz and the Brillouin shift of acetone was measured to be 2.63 GHz. It is important to mention that the characteristic PSF of the V-type atomic line monochromator is visible at the Brillouin frequencies of acetone and methanol because the PSF peaks have a frequency separation greater than the natural Brillouin linewidths of acetone and methanol [62].

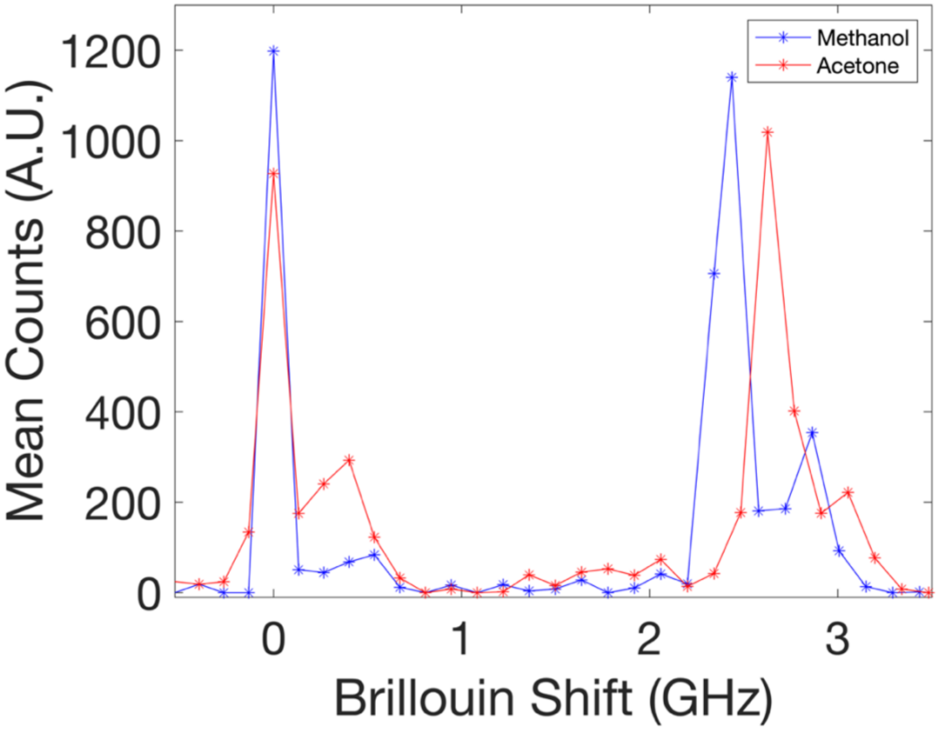

Figure 4.7. Brillouin spectra of methanol (blue) and acetone (red) acquired using the full-field Brillouin microscope.

4.2.2 Microscope characterizations

The spatial resolution performances of the full-field Brillouin spectrometer were also characterized. The spatial resolution in the lateral direction (x-direction) is determined by the pixel size of the image, which depends on the overall magnification of the imaging system. With a detector pixel size of 16 μm and an image magnification of 1.4X, the image pixel size should be 11.43 μm. To measure the image pixel size, a knife edge was placed in front of the sample cuvette on a translational stage. The stage was translated in the x-direction in increments of 500 μm, revealing the pixels in the imaged Brillouin signal line. The knife edge displacement versus the number of pixels revealed in the laser line is shown in Fig. 4.8. The data was fit linearly (blue-dashed line), to show that the image pixel size is 11.56 µm.

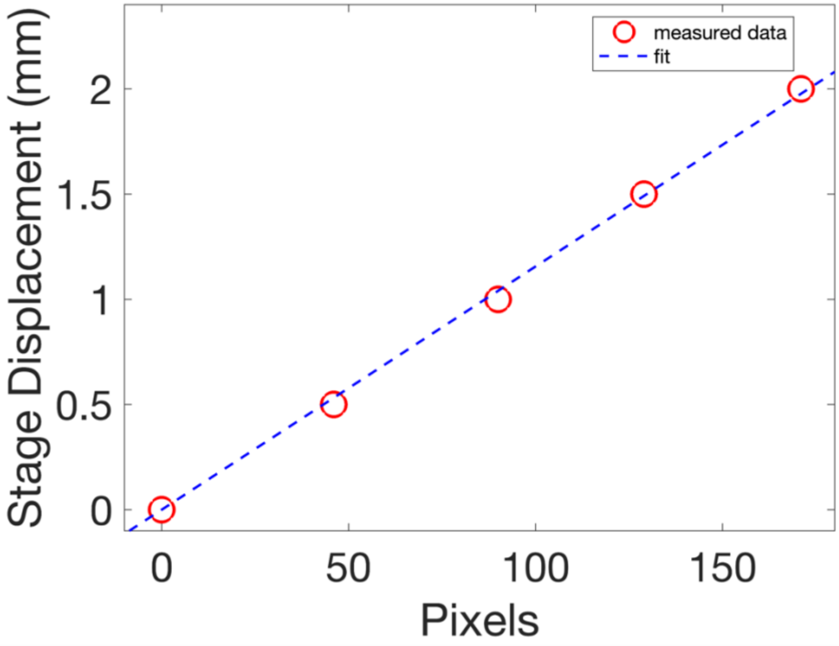

Figure 4.8. Spatial resolution performance of the full-field Brillouin microscope. The slope of the linear fit is 0.01156.

The noise performances of the full-field Brillouin microscope were evaluated by measuring the signal-to-noise ratio (SNR) of the device. The SNR was measured by changing the incident laser power while keeping the camera exposure time constant. The frequency of the incident laser was detuned to the acetone Brillouin shift frequency and optimized for maximum pixel intensity. For each incident laser power, a series of 200 full-field acetone Brillouin images were taken while the exposure time was kept constant at 500 ms per image. The incident power was varied from 99 to 335 mW.

Figure 4.9(a) shows an example of a full-field acetone Brillouin image taken for SNR measurement. The maximum cross-sectional intensity (dashed line) was taken from the 200 images, and 50 consecutive images from the original 200 were used to calculate the SNR to reduce variance. The SNR as a function of incident laser power on a log-log scale is shown in Fig. 4.9(b). Between incident laser powers of 100 and 150 mW, the Brillouin signal is at the noise floor of the camera dark noise and, thus, the SNR is constant. At incident laser powers greater than 150 mW, the SNR begins to increase. The dashed black line is a linear fit to the SNR data of .5083 slope, indicating that the full-field Brillouin microscope operates in the shot-noise limited regime.

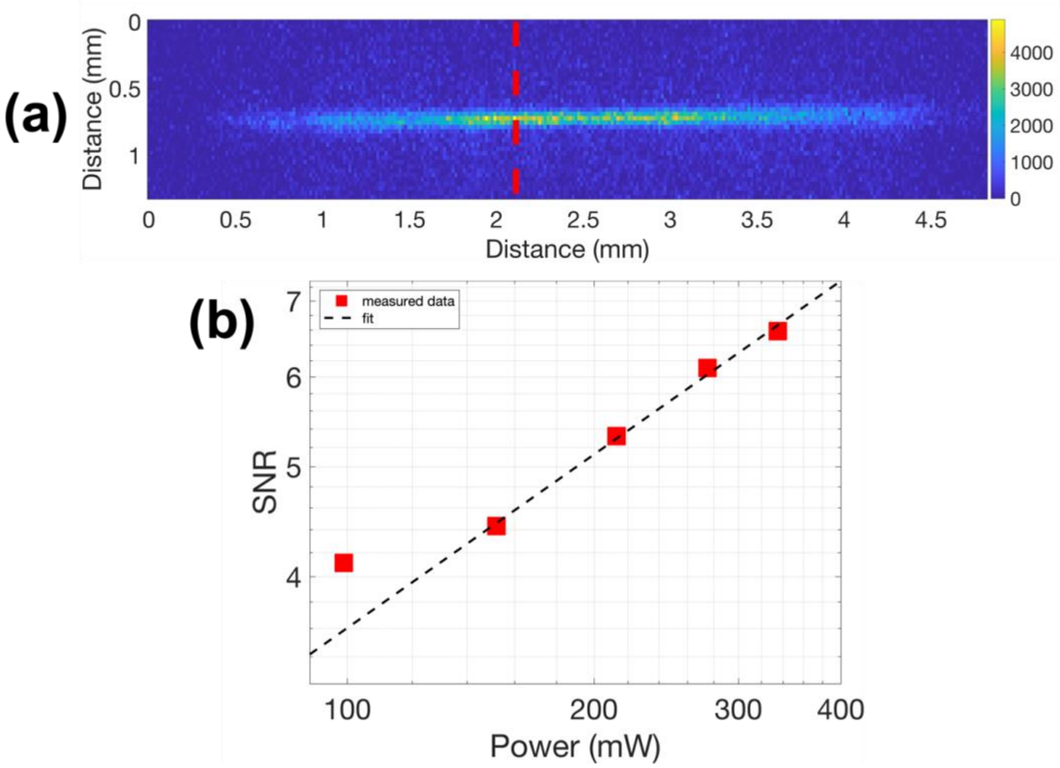

Figure 4.9. Noise behavior of full-field Brillouin imaging system. (a) Full-field Brillouin image of methanol sample. (b) Signal-to-noise ratio (SNR) versus incident laser power incident to the sample cuvette on a log-log scale. The fitted line has a slope of 0.5083.

The present application of line-illumination in the full-field Brillouin microscope restricts spectral analysis to 1-D. Although the current configuration is in place, the V-type atomic line monochromator exhibits the capability for spectral analysis in both x- and y-directions, facilitating

two-dimensional (2-D) multiplexing. The ability for 2D spectral analysis is evident when modifying the angle of mirror M1 (Fig. 4.3), positioned before the illumination objective. A representative image of line illumination used for full-field Brillouin imaging is shown in Fig. 4.10(a). The incident laser power is 318 mW and the acquisition time is 200 ms. The incident laser frequency was detuned to the methanol Brillouin shift frequency and the pump laser is locked at the D_1 ^{87}Rb $5^2S_{1/2}(F_g = 2) \rightarrow 5^2P_{1/2}(F_e = 2)$ transition. The Brillouin signal line can be shifted up and down in the axial direction (z-direction) by changing the angle of M1. Figure 4.10(b) displays a composite image that incorporates multiple images taken at various arbitrary angles of mirror M1. Each constituent image within the composite has the same acquisition parameters as the image in Fig. 4.10(a). By coarsely adjusting the angle of the mirror, it becomes possible to scan the 1-D multiplexed Brillouin signal over an approximate range of 2.4 mm in the axial direction.

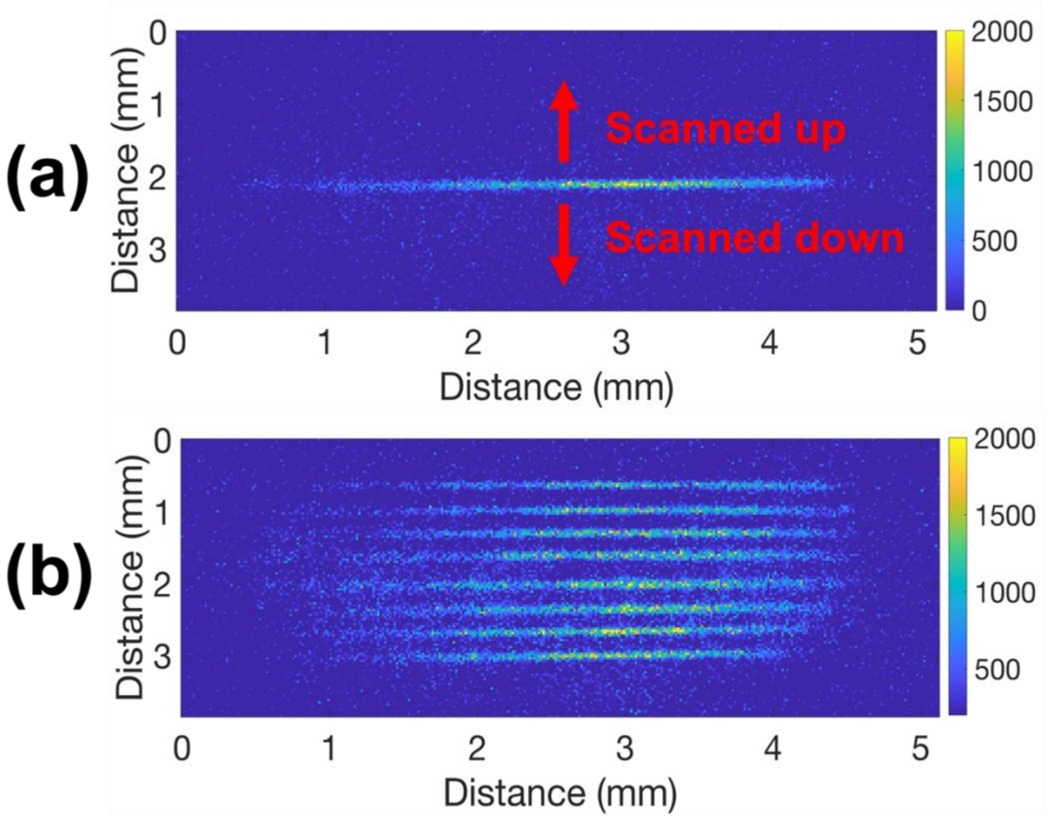

Figure 4.10. Demonstration of 2D spectral analysis using the full-field Brillouin microscope. (a) Example of acetone Brillouin image using the full-field Brillouin microscope. (b) Composite image of multiple acetone full-field Brillouin images, each image corresponding to different positions of the line illumination in the axial direction.

4.3 Conclusions

In summary, we have demonstrated full-field Brillouin scattering measurements in clear liquid samples using an atomic line monochromator. The V-type atomic line monochromator was innovated to have less pump-background noise than earlier implementations of the device, making it a feasible approach for full-field Brillouin imaging.

From previous experiments where the exposure time was 500 ms exposure and 200 pixels multiplexed, the spectral pixel acquisition time is 2.5 ms/pixel in clear liquid samples. The acquisition time can be further improved by increasing the magnification of the imaging system so that the line illumination can fill the entire area of the camera. For example, since the detector size is 512x512 pixels, a 2-fold increase in magnification can improve the multiplexing by a factor of 2.5. Cameras with even larger detector sizes exist, meaning that the pixel acquisition time can be further improved by switching the detector.

The illumination arm of the full-field Brillouin microscope can be modified to allow for 2-D image construction. For example, M1 (Fig. 4.3) can be replaced with a galvanometer mirror to scan the laser beam in the axial direction. Alternatively, a cylindrical lens can be placed in the illumination path to create a light-sheet, generating Brillouin photons in the x- and y-direction simultaneously for spectral analysis. However, the speed benefits of multiplexing are only true in the propagation direction of the laser, so there is no multiplexing benefit in the other spatial direction.

For future Brillouin measurements in biological samples, higher spectral extinction may be necessary. The water Brillouin shift at 90^o detection and 780.24 nm incident laser light is ~3.5 GHz. If the incident laser wavelength is locked at ^{87}Rb $5^2S_{1/2}(F_g = 2) \rightarrow 5^2P_{3/2}(F'_e = 3)$ transition, the water Brillouin peak will occur within the $(F_g=2)$ band. An ^{85}Rb atomic vapor notch filter can be placed within the microscope to provide an additional ~35 dB rejection of light in a range of ~500 MHz. In combination with the spectral extinction provided by the linear polarizers, the overall extinction of the full-field Brillouin microscope would be ~85 dB, which is sufficient for Brillouin measurements of biological samples [3,90].

In conclusion, we have expanded the Brillouin microscopy toolbox by evaluating the performances and unique characteristics of atomic line monochromators. This technology has the potential to significantly reduce the Brillouin image acquisition time in biological samples.

Chapter 5

Summary of Scientific Contributions and Outlook

5.1 Summary of Scientific Contributions

The results from my work have shifted the research paradigms of the Brillouin microscopy field. Brillouin microscopy is an emerging imaging modality where the contrast mechanism is the frequency shift of Brillouin scattered light, allowing for mechanical characterizations of tissues and cells. Due to the low frequency shift of Brillouin scattered light and the low Brillouin scattering cross-section, Brillouin microscopes require state-of-the-art spectrometers that possess high spectral resolution and high transmission for spectral analysis. Etalons such as Fabry-Pérot and VIPA etalons have dominated the Brillouin spectroscopy field for years because they possess the transmission and spectral resolution performances to measure Brillouin scattered light, however, these etalon-based spectrometers have begun to reach the limit of their acquisition capabilities for biological samples. Although the line scan Brillouin spectrometer was innovated to increase the Brillouin acquisition speed with 1D pixel multiplexing using a VIPA-based spectrometer, using etalons for pixel multiplexing is complicated by the optical aberrations introduced by the imaging system of the spectrometer, leading to throughput inefficiencies of the spectral information. Furthermore, 2D pixel multiplexing could further improve Brillouin imaging speeds, but etalons are incapable of 2D pixel multiplexing due to the angular dispersion of spectral components inside the etalon cavity. To realize the 2D multiplexing of Brillouin signal, a high-resolution, high-transmission spectrometer with spectral analysis capabilities that do not use angular dispersion will need to be created. In Chapter 2, I identified an atomic line monochromator based on the LICD effect as a candidate technology for full-field spectroscopy at high resolutions. After completing a pump irradiance and atomic vapor cell temperature characterization of the device, the transmission (16%) and the spectral resolution (80 MHz) were found to be competitive with current Brillouin spectrometers and, therefore, sufficient for measuring spontaneous Brillouin scattered light. By scanning the pump laser frequency and taking advantage of the hot atomic vapor Doppler-broadening, the LICD atomic line monochromator transmission window can be detuned over a ~500 MHz frequency range for spectral analysis. Finally, I demonstrated full-field spectral analysis by transmitting whole images of a USAF test target through the atomic line monochromator. In 2022, I presented this holistic characterization of the developed LICD atomic line monochromator at SPIE Photonics West in San Francisco, CA. In 2023, this work was published in *Optics Express*.

In Chapter 3, I created the first practical implementation of an LICD atomic line monochromator for measuring spontaneous Brillouin scattered light in Chapter 3. The LICD atomic line monochromator built in Chapter 2 suffered from significant background noise arising from the pump laser reflecting off the window of the atomic vapor cell inside of the setup and into the detector. The pump background noise is orders of magnitude higher than the spontaneous Brillouin signal, making it difficult to measure Brillouin scattered light at incident laser powers typically used for biological samples. The atomic line monochromator built in Chapter 3 is based on a ladder-type pumping scheme where the pump laser and the signal frequency operate at two different atomic transitions and, as a result, different frequencies. In this way, I incorporated a commercial bandpass filter that provided -60 dB rejection of the pump background noise and 95% transmission of the signal. The ladder-type atomic line monochromator possesses 13% transmission and 220 MHz linewidth, similar performances to the device developed in Chapter 2. To demonstrate the proof-of-principle, the ladder-type atomic line monochromator was combined with a confocal microscope to measure spontaneous Brillouin scattered light in clear liquids. The central frequency of the atomic line monochromator bandpass was fixed and the incident laser frequency was swept, leading to the Brillouin signal being scanned through the monochromator bandpass. This work is the first demonstration of an LICD atomic line monochromator used for the spectral analysis of Brillouin scattered light. In 2024, this work was presented at SPIE Photonics West in San Francisco, CA.

In Chapter 4, I built the first full-field Brillouin microscope using line illumination and an atomic line monochromator based on a V-type pumping scheme. With the V-type pumping scheme, the difference between the pump laser and signal frequencies was 15 nm, nearly 3.75 times greater than the frequency difference between the pump laser and signal frequencies from Chapter 3. The V-type atomic line monochromator possesses nearly 10% transmission and 80 MHz spectral resolution. After characterizing the monochromator, line illumination and orthogonal detection were used for the first demonstration of pixel multiplexing of Brillouin photons using an atomic line monochromator. Like the device from Chapter 3, the V-type atomic line monochromator bandpass frequency was fixed and the frequency of the laser incident to the sample was swept, sweeping the Brillouin signal through the atomic line monochromator transmission window. Brillouin spectra of methanol and acetone were acquired using the full-field Brillouin microscope. Furthermore, I showed that position Brillouin photons can be analyzed in the full imaging field by physically scanning the incident laser.

Overall, my graduate research has led to one first-authored publication and another first-authored publication in preparation. I am also a co-inventor of a patent on the development of full-field Brillouin microscopy systems and methods. I have presented my research twice at SPIE Photonics West, one of the largest international conferences for optics research. The University of Maryland acknowledged my work by awarding me the Ann G. Wiley Dissertation Fellowship.

A list of scientific contributions is summarized below:

1. Chapter 2:
    a. First full characterization of the LICD atomic line monochromator image transmission properties
        i. By expanding the pump laser with a telescope or increasing the laser intensity, the resolution of an image transmitted through the atomic line monochromator approaches the resolution of the imaging system
2. Chapter 3:
    a. First Brillouin spectrometer based on the LICD effect

        i. The ladder-type optical pumping scheme allows for edge filtering of the pump back-reflection noise
        ii. The ladder-type atomic line monochromator 13% transmission and ~220 MHz resolution allows Brillouin measurements in clear liquids
3. Chapter 4:
    a. Shot-noise limited Brillouin measurements in clear liquids using an atomic line monochromator
        i. The V-type pumping scheme facilitates a 15 nm difference between the pump laser and signal wavelengths, enabling effective rejection of the pump background noise
    b. First Brillouin spectrometer capable of spectral analysis in the full-field
        i. Using line-illumination, Brillouin photons were multiplexed for 1D spectral analysis
        ii. Scanning the position of the illumination laser allows for spectral analysis in 2D

5.2 Future Directions

Although full-field Brillouin microscopy has been realized with an atomic line monochromator, additional improvements will have to be made to extend the technology for measuring spontaneous Brillouin scattering in biological samples. With an acquisition time of 2.5 ms/pixel in acetone and methanol, the current device is too slow. Improving the monochromator transmission will reduce the pixel acquisition time. The 10% transmission arises from the V-type pumping scheme using an open system, making it so that the pump transition is never truly saturated. In the future, using a V-type pumping scheme with a “closed” atomic transition [90-95], i.e. all the electrons being optically pumped do not fall to a ground state that is separate from the atomic transition, will help increase the transmission of the atomic line monochromator. A proposed alternative for a new V-type pumping scheme would be switching the two laser wavelengths. The pump laser would be resonant with the D_2 ^{87}Rb $5^2S_{1/2}(F_g = 2) \rightarrow 5^2P_{3/2}(F'_e = 3)$ at 780.24 nm and the incident laser would be resonant with the D_1 ^{87}Rb $5^2S_{1/2}(F_g = 2) \rightarrow 5^2P_{1/2}(F_e = 2)$ transition at 794.98 nm. This V-type pumping scheme (fig. 7.1) has been previously used for two-color polarization spectroscopy [81], but it can be also used to realize an atomic line monochromator. Because the D_2 transition is closed, the transition can be completely saturated, leading to a higher signal transmission for the atomic line monochromator. At the time of this dissertation, we were unable to use this V-type pumping scheme because we did not have a laser amplifier that could increase the incident laser power at 794.98 nm for Brillouin measurements. Furthermore, we did not possess Bragg filters designed to clean the laser line at 794.98 nm.

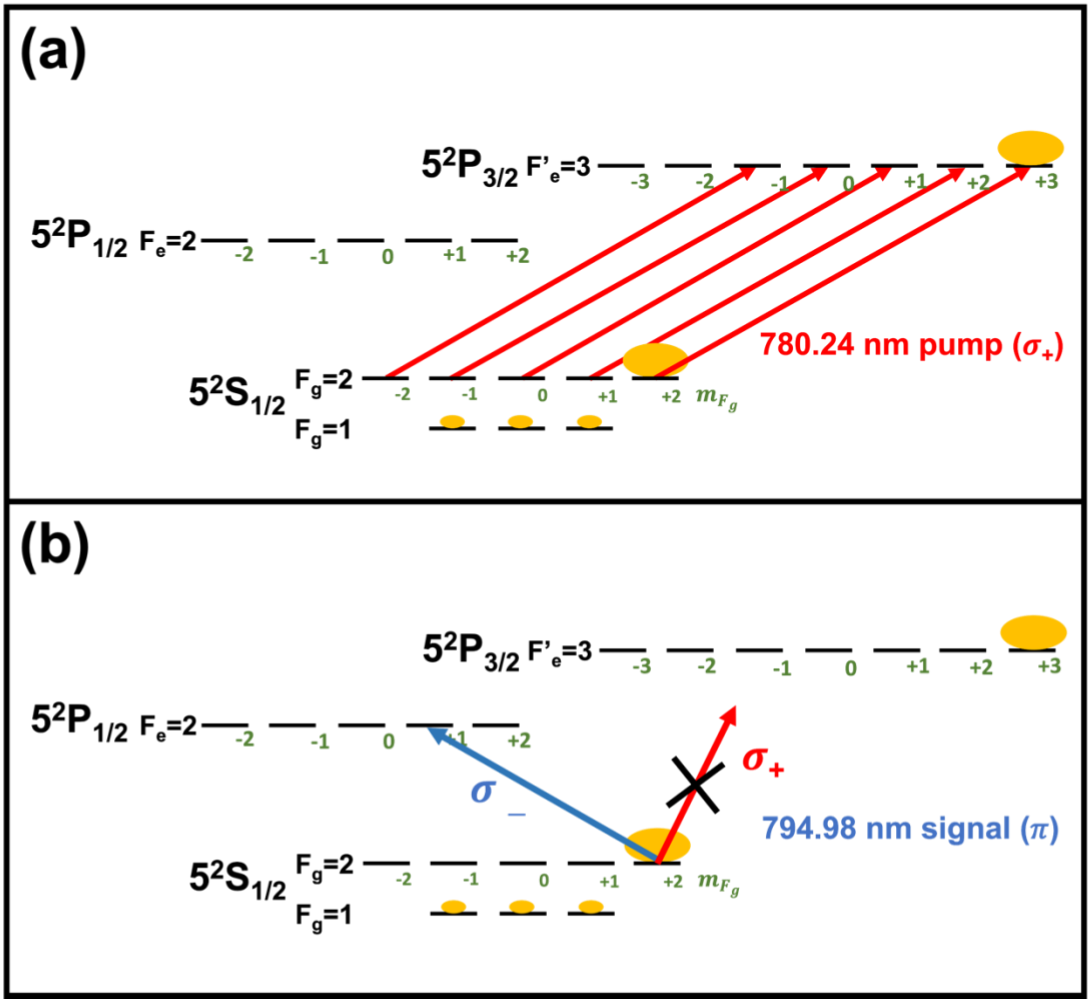

Figure 5.1. Alternative pumping scheme for the V-type atomic line monochromator. (a) A σ+-polarized pump laser (solid red arrow) saturates the $5^2S_{1/2}$ (F_g=2, m_{Fg} = 2)→$5^2P_{3/2}$ (F'_e=3, $m_{F'e}$ = 3) magnetic sublevel transition at 780.24 nm. (b) The π-polarized probe laser (blue arrows) is resonant with the $5^2S_{1/2}$ (F_g=2)→$5^2P_{1/2}$ (F_e=2) transitions at 794.98 nm. The left circular polarization component of the probe laser (blue solid arrow) is normally absorbed, but the right circular component (red arrow) will not be absorbed.

Bibliography

1. Brillouin L (1922). “Diffusion de la lumière et des rayons X par un corps transparent homogène.” *Annales De Physique*. Vol. 9, No. 17:88–122.
2. Gross E (1930). “Change of wave-length of light due to elastic heat waves of scattering in liquids”. *Nature*. 126(3171), 201–202.
3. Scarcelli G, Yun SH (2008). “Confocal Brillouin microscopy for three-dimensional mechanical imaging.” *Nature Photonics*, 2, 39–43.
4. Scarcelli G, Polacheck WJ, Nia HT, Patel K, Grodzinsky AJ, Kamm RD, and Yun SH (2015). “Noncontact three-dimensional mapping of intracellular hydromechanical properties by Brillouin microscopy.” *Nature Methods*, 12(12),1132–1134.
5. Sandercock JR (1970). “Brillouin scattering study of SbSI using a double-passed, stabilised scanning interferometer.” *Optics Communications*. 2(2), 73–76.
6. Lindsay SM, Anderson MW, Sandercock JR (1981). “Construction and alignment of a high performance multipass vernier tandem Fabry–Pérot interferometer”. *Review of Scientific Instruments*, 52(10), 1478–1486.
7. Scarcelli G, Yun SH (2011). “Multistage VIPA etalons for high-extinction parallel Brillouin spectroscopy.” *Optics Express* 19(11), 10913–10922.
8. Zhang J, Fiore A, Yun SH, Kim H, Scarcelli G (2016). “Line-scanning Brillouin microscopy for rapid non-invasive mechanical imaging.” *Scientific Reports*, 6, 35398–35398.
9. Zhang J, Nikolic M, Tanner K, and Scarcelli G (2023). “Rapid biomechanical imaging at low irradiation level via dual line-scanning Brillouin microscopy.” *Nature Methods*, 20(5), 677–681.
10. Bevilacqua C, Gomez JM, Fiuza U-M, Chan CJ, Wang L, Hambura S, Eguren M, Ellenberg J, Diz-Muñoz A, Leptin M, and Prevedel R (2023). “High-resolution line-scan Brillouin microscopy for live imaging of mechanical properties during embryo development.” *Nature Methods*, 20(5), 755-760.
11. Muller W, Schmitt M, Popp J, Heintzmann R, and Kielhorn M (2016). “Light-sheet Raman micro-spectroscopy”. *Optica*, *3*(4), 452–457.
12. Subedi NR, Yaraghi S, Jung PS, Kukal G, McDonald AG, Christodoulides DN, and Vasdekis AE (2021). “Airy light-sheet Raman imaging.” *Optics Express*, 29(20), 31941-31951.
13. Fantuzzi EM, Heuke S, Labouesse S, Gudavičius D, Bartels R, Sentenac A, and Rigneault H (2023). “Wide-field coherent anti-stokes Raman scattering microscopy using random illuminations.” *Nature Photonics*, 17(12), 1097–1104.
14. Rocha-Mendoza I, Licea-Rodriguez J, Marro M, Olarte OE, Plata-Sanchez M, and Loza-Alvarez P (2015). “Rapid spontaneous Raman light sheet microscopy using cw-lasers and tunable filters.” *Biomedical Optics Express*, 6(9), 3449–61.
15. Jahr W, Schmid B, Schmied C, Fahrbach FO, and Huisken J (2015). “Hyperspectral light sheet microscopy.” *Nature Communications*, 6, 7990–7990.

16. Morizet J, Chow D, Wijesinghe P, Schartner E, Dwapanyin G, Dubost N, Bruce GD, Anckaert E, Dunning K, and Dholakia K (2023). "UVA hyperspectral light-sheet microscopy for volumetric metabolic imaging: application to preimplantation embryo development." *ACS Photonics*, 10(12), 4177–4187.
17. Yin B, Alvarez L, and Shay TM (1994). "The Rb 780-nanometer Faraday anomalous dispersion optical filter: Theory and experiment." *Telecommunications and Data Acquisition Report*, 116, 71–85.
18. Yong Y, Xuewu C, Faquan L, Xiong H, Xin L, and Shunsheng G (2011). "A flat spectral Faraday filter for sodium lidar." *Optics Letters*, 36(7), 1302-1304.
19. Rudolf A, and Walther T (2014). "Laboratory demonstration of a Brillouin lidar to remotely measure temperature profiles of the ocean." *Optical Engineering*, 53(5), 475–481.
20. Friedman JS, Maldonado-Nieves D, González I, Lautenbach J, Chu X, Smith JA, and Huang W (2012). "High spectral resolution test and calibration of an ultra-narrowband faraday anomalous dispersion optical filter for use in daytime mesospheric resonance Doppler lidar." *Journal of Atmospheric and Solar-Terrestrial Physics*, 80, 187-194.
21. Yang Z, Guan X, Luo B, Yin L, Gao G and Chen J (2019), "Ambient Light Suppressed Free Space Optical Communication System based on FADOF." *2019 18th International Conference on Optical Communications and Networks (ICOCN)*, Huangshan, China, pp. 1-3.
22. Junxiong T, Qingji W, Yimin L, Liang Z, Jianhua G, Minghao D, Jiankun K, and Lemin Z (1995). "Experimental study of a model digital space optical communication system with new quantum devices." *Applied Optics*, 34(15), 2619–22.
23. Chang P, Peng H, Zhang S, Chen Z, Luo B, Chen J, and Guo H (2017). "A faraday laser lasing on Rb 1529 nm transition." *Scientific Reports*, 7(1), 8995-8995.
24. Duo P, Xiaobo X, Haosen S, Bin L, Jingbiao C, and Hong G (2016). "Hollow cathode lamp based faraday anomalous dispersion optical filter." *Scientific Reports, 6*.
25. Tang H, Zhao H, Zhang D, Li L, Yang W, Han K, Yang Z, Wang H, and Xu X (2022). "Polarization insensitive efficient ultra-narrow diode laser strictly locked by a Faraday filter." *Optics Express*, 30(16), 29772-29780.
26. Foot CJ. *Atomic Physics*. Oxford: Oxford University Press; 2005.
27. Yeh P. "Dispersive magnetooptic filters (1982)." *Applied Optics*, 21(11), 2069-2075.
28. Liu S, Zhang Y, Wu H, Yuan P (2012). "Ultra-narrow bandwidth atomic filter based on optical-pumping-induced dichroism realized by selectively saturated absorption." *Optics Communications*, 285(6), 1181–1184.
29. Cerè A, Parigi V, Abad M, Wolfgramm F, Predojevic´, AP, and Mitchell MW (2009). "Narrowband tunable filter based on velocity-selective optical pumping in an atomic vapor." *Optics Letters*, 34(7), 1012-1014.
30. Steck DA. "Rubidium 87 D Line Data," available online at http://steck.us/alkalidata (revision 2.3. 2, 10 September 2023)

31. Demtröder W (2008). *Laser spectroscopy* (4th ed., Vol. Vol. 2, experimental techniques). Springer-Verlag.
32. Demtröder W (2008). *Laser spectroscopy: Basic Principles* (4th ed., Vol. 1). Springer-Verlag.
33. Pedrotti FL, Pedrotti LM, and Pedrotti LS (2018). *Introduction to optics* (Third edition [re-issued]). Cambridge University Press.
34. Svelto O, and Hanna DC (2010). *Principles of Lasers* (5th ed., Ser. 2010 springer e-books). Springer.
35. Gayen S. K., Billmers R. I., Contarino V. M., Squicciarini M. F., Scharpf W. J., Yang G., Herczfeld P. R., and Allocca D. M. (1995). "Induced-dichroism-excited atomic line filter at 532 nm". *Optics Letters*, *20*(12), 1427–9.
36. Griffiths DJ (2005). *Introduction to quantum mechanics* (2nd ed.). Pearson Prentice Hall.
37. Steck DA. "Rubidium 87 D Line Data," available online at http://steck.us/alkalidata (revision 2.3. 2, 10 September 2023)
38. Axner O, Gustafsson J, Omenetto N, and Winefordner, JD (2004). "Line strengths, a-factors and absorption cross-sections for fine structure lines in multiplets and hyperfine structure components in lines in atomic spectrometry—a user's guide." *Spectrochimica Acta Part B: Atomic Spectroscopy*, 59(1), 1–39.
39. Citron ML, Gray HR, Gabel CW, and Stroud CR (1977). "Experimental study of power broadening in a two-level atom." *Physical Review A*, 16(4), 1507–1512.
40. Sherlock BE, and Hughes IG (2009). "How weak is a weak probe in laser spectroscopy?" *American Journal of Physics*, 77(2), 111–115.
41. Svelto O, and Hanna DC (2010). *Principles of Lasers* (5th ed., Ser. 2010 springer e-books). Springer.
42. Inguscio M, and Fallani L (2013). *Atomic physics : precise measurements and ultracold matter* (First). Oxford University Press.
43. Arie A, Lissak B, and Tur M (1999). "Static fiber-bragg grating strain sensing using frequency-locked lasers." *Journal of Lightwave Technology*, 17(10).
44. Wang, W., Akulshin, A. M., Ohtsu, M., & OFC/NFOEC 2008. 2008 Optical Fiber Communication Conference/National Fiber Optic Engineers Conference San Diego, CA, USA. (1994). "Pump-probe spectroscopy in potassium using an AlGaAs laser and the second-harmonic generation of an InGaAsP laser for frequency stabilization and linking." *Ieee Photonics Technology Letters*, 6(1).
45. Bruner A, Arie A, Arbore MA, and Fejer MM (1998). "Frequency stabilization of a diode laser at 1540 nm by locking to sub-doppler lines of Potassium at 770 nm." *Applied Optics*, 37(6), 1049–52.
46. Tiecke TG, "Properties of Potassium" available online at https://tobiastiecke.nl/archive
47. Light RA, Johnston NS, Somekh MG, Pitter MC, Smith RJ, and Optical Sensors 2011; and Photonic Crystal Fibers V Prague, CZE 2011 04 18 - 2011 04 20. (2011). "Cmos lock-in optical sensor for parallel detection in pump-probe systems." *Proceedings of Spie - the International Society for Optical Engineering, 8073.*

48. Ivanov R, Villa J, de la Rosa I, and Marín E (2011). "An alternative differential method of femtosecond pump-probe examination of materials." *Optics Express*, 19(12), 11290–8.
49. Giulia Z, and Giuliano S (2022). "Localization-Assisted Stimulated Brillouin Scattering Spectroscopy." *APL Photonics*, 7(5), 056101–056101.
50. Westergaard PG, Lassen M, and Petersen JC (2015). "Differential high-resolution stimulated CW Raman spectroscopy of hydrogen in a hollow-core fiber." *Optics* Express 23, 16320-16328.
51. Uhland D, Rendler T, Widmann M, Lee S-Y, Wrachtrup J, and Gerhardt I (2015). "Single molecule DNA detection with an atomic vapor notch filter." *EPJ Quantum Technology*, 2, 20.
52. Heifetz A, Agarwal A, Cardoso GC, Gopal V, Kumar P, and Shahriar MS (2004). "Super efficient absorption filter for quantum memory using atomic ensembles in a vapor." *Optics Communications*, 232(1), 289–293.
53. Xue X, Janisch C, Chen Y, Liu Z, and Chen J (2016). "Low-frequency shift raman spectroscopy using atomic filters." *Optics Letters*, 41(22), 5397–5400.
54. Meng Z, Traverso AJ, and Yakovlev VV (2014). "Background clean-up in brillouin micro-spectroscopy of scattering medium." *Optics Express*, 22(5), 5410–5415.
55. Hair JW, Caldwell LM, Krueger DA, and She CY (2001). "High-spectral-resolution lidar with iodine-vapor filters: measurement of atmospheric-state and aerosol profiles." *Applied Optics*, 40(30), 5280–5294.
56. He Z, Zhang Y, Liu S, and Yuan P (2007). "Transmission characteristics of an excited-state induced dispersion optical filter of rubidium at 775.9 nm." *Chinese Optics Letters*, 5(5), 252–254.
57. Almuhawish NF, Chen S, Downes LA, Jamieson MJ, MacKellar AR, and Weatherill KJ (2021). "Polarization spectroscopy of an excited state transition in rubidium." *OSA Continuum*, 4(10), 2598–2598.
58. Gea-Banacloche J, Li Y, Jin S, and Xiao M (1995). "Electromagnetically induced transparency in ladder-type inhomogeneously broadened media: theory and experiment." *Physical Review A; (United States)*, 51(1), 576–584.
59. Moon, HS, Lee L, and Kim JB (2008). "Double resonance optical pumping effects in electromagnetically induced transparency." *Optics Express*, 16(16), 12163–70.
60. Noh H-R, and Moon HS (2021). "Four-wave mixing in a ladder configuration of warm ^{87}Rb atoms: a theoretical study," *Optics Express*, 29, 6495-6508.
61. Kramida A, Ralchenko Y, Reader J, NIST ASD Team. NIST Atomic Spectra Database. Version 510 2022.
62. Boyd RW. *Nonlinear optics* (3rd ed.). Academic Press (2008).
63. Hutchins R, Zanini G, and Scarcelli G (2023). "Full-field optical spectroscopy at a high spectral resolution using atomic vapors." *Optics Express*, 31(3), 4334–4346.
64. Vitanov NV, Shore BW, Yatsenko L, Böhmer K, Halfmann T, Rickes T, and Bergmann, K (2001). "Power broadening revisited: theory and experiment," *Optics Communications*, 199(1), 117–126.

65. He Z, Zhang Y, Wu H, Yuan P, and Liu S (2009). "Theoretical model for an atomic optical filter based on optical anisotropy." *Journal of the Optical Society of America. Part B, Optical Physics*, 26(9).
66. Gray HR, and Stroud CR (1978). "Autler-Townes effect in double optical resonance." *Optics Communications*, 25(3), 359–362.
67. Hao L, Jiao Y, Xue Y, Han X, Bai S, Zhao J, and Raithel G (2018). "Transition from electromagnetically induced transparency to Autler-Townes splitting in cold cesium atoms." *New Journal of Physics*, 20(7).
68. Carr C, Adams CS, and Weatherill KJ (2012). "Polarization spectroscopy of an excited state transition." *Optics Letters*, 37(1), 118–20.
69. Haynes WM, Lide DR. *Handbook of Chemistry and Physics* (95th ed). CRC Press (2014).
70. Mattana S, Mattarelli M, Urbanelli L, Sagini K, Emiliani C, Serra MD, Fioretto D, and Caponi S (2018). "Non-contact mechanical and chemical analysis of single living cells by micro-spectroscopic techniques." *Light: Science & Applications*, 7, 17139–17139.
71. Sauerer B, Craddock PR, AlJohani MD, Alsamadony KL, and Abdallah W (2017). "Fast and accurate shale maturity determination by Raman spectroscopy measurement with minimal sample preparation." *International Journal of Coal Geology*, 173, 150–157.
72. Jansson, PA (1997). *Deconvolution of images and spectra* (2nd ed.). Academic Press.
73. Caponi S, Fioretto D, and Mattarelli M (2020). "On the actual spatial resolution of Brillouin Imaging." *Optics Letters*, 45, 1063-1066.
74. Pezzotti G (2021). "Raman spectroscopy in cell biology and microbiology." *Journal of Raman Spectroscopy*, 52(12), 2348–2443.
75. Milonni PW, and Eberly JH (2010). *Laser physics*. John Wiley & Sons.
76. Yariv A. (1989). *Quantum electronics* (3rd ed.). Wiley.
77. Cohen RD, Mullarkey CA, Howell JC, and Katz N (2018). "Polarization-independent atomic prism filter for removing amplified spontaneous emission." *Applied Optics*, 57(16), 4472–4476.
78. Pettine J, Zhu M, and Anderson DA (2020). "Self-adaptive amplified spontaneous emission suppression with a photorefractive two-beam coupling filter." *Optics Letters*, 45, 6258-6261.
79. Nikolić M and Scarcelli G (2019). "Long-term Brillouin imaging of live cells with reduced absorption-mediated damage at 660nm wavelength." *Biomedical Optics Express*, 10(4) 1567-1580.
80. Simin P, Xinbao L, Jiajun L, Yaru X, Jiang T, Sheng M, Ping-Heng T, and Jun Z (2022). "Brillouin light scattering of halide double perovskite." *Advanced Photonics Research*, 3(8).
81. Cha EH, Jeong T, and Noh H-R (2014). "Two-color polarization spectroscopy in V-type configuration in Rubidium." *Optics Communications*, 326, 175–179.
82. Braunstein D, and Shuker R (2001). "Absorption with inversion and amplification without inversion in a coherently prepared V system: a dressed-state approach." *Physical Review -Series A-*, 64, 053812–053812.

83. Das A, Das BA, Bhattacharyya D, and De S (2021). "Effects of probe ellipticity and longitudinal magnetic field on the polarization rotation in a coherently prepared atomic medium." *OSA Continuum*, 105-120.
84. de Echaniz SR, Greentree AD, Durrant AV, Segal DM, Marangos JP, and Vaccaro JA (2001). "Observations of a doubly driven V system probed to a fourth level in laser-cooled Rubidium." *Physical Review -Series A-*, 64, 013812–013812.
85. Eisberg RM, and Resnick R (1985). *Quantum physics of atoms, molecules, solids, nuclei, and particles* (2nd ed.). Wiley.
86. Siegman AE (1986). *Lasers*. University Science Books.
87. Sydoryk I, Bezuglov NN, Beterov II, Miculis K, Saks E, Janovs A, Spels P, and Ekers A (2008). "Broadening and intensity redistribution in the Na (3p) hyperfine excitation spectra due to optical pumping in the weak excitation limit." *Physical Review A - Atomic, Molecular, and Optical Physics*, 77(4).
88. Entin VM, Ryabtsev II, Boguslavsky AE, and Brzhazovsky YV (2002). "Laser spectroscopy of spontaneous coherence transfer and optically induced polarization rotation in ^{87}Rb." *Optics Communications*, 207(1), 201–208.
89. Vasil'ev VV, Velichanskii VL, Zibrov SA, Sivak AV, Brazhnikov DV, Taichenachev AV, and Yudin VI (2011). "Dual structure of saturated absorption resonance at an open atomic transition." *Journal of Experimental and Theoretical Physics*, 112(5), 770–779.
90. Fiore A, Zhang J, Shao P, Yun SH, and Scarcelli G (2016). "High-extinction virtually imaged phased array-based Brillouin spectroscopy of turbid biological media." *Applied Physics Letters*, 108(20), 203701–203701.
91. Pearman CP, Adams CS, Cox SG, Griffin PF, Smith DA, Hughes IG (2002). "Polarization spectroscopy of a closed atomic transition: applications to laser frequency locking." *Journal of physics B: Atomic, Molecular and Optical Physics*, 35(24), 5141-5151.
92. Jeong J, Lee S, Hwang S, Baek J, Noh H-R, Moon G (2021). "Theoretical and experimental study of optimization of polarization spectroscopy for the D_2 closed transition line of ^{87}Rb atoms." *Applied sciences*, 11(16), 7219-7219.
93. Harris ML, Adams CS, Cornish SL, McLeod IC, Tarleton E, and Hughes IG (2006). "Polarization spectroscopy in rubidium and cesium". *Physical Review. A*, 73(6).
94. Zhang J, Wei D, Xie C, and Peng K (2003). "Characteristics of absorption and dispersion for rubidium D_2 lines with the modulation transfer spectrum." *Optics Express*, 11(11), 1338–44.
95. Pahwa K, Mudarikwa L, and Goldwin J (2012). "Polarization spectroscopy and magnetically-induced dichroism of the potassium D_2 lines," *Optics Express*, 20, 17456-17466.